Journal of Materials Processing Tech. 320 (2023) 118104

Contents lists available at ScienceDirect

Journal of Materials Processing Tech.

journal homepage: www.elsevier.com/locate/jmatprotec

Cracking behavior of Ti-48Al-2Cr-2Nb alloy in powder bed fusion electron beam melting process

Seungkyun Yim [a,*], Kenta Aoyagi [a,*], Huakang Bian [a], Keiji Yanagihara [a], Yuchao Lei [a], Shin-ichi Kitamura [b], Hironobu Manabe [b], Yohei Daino [c], Kenta Yamanaka [a], Akihiko Chiba [a,*]

[a] Institute for Materials Research, Tohoku University, 2–1-1 Katahira, Sendai, Miyagi 980–8577, Japan
[b] Advanced & Fundamental Technology Center, JEOL Ltd., Akishima, Tokyo 196–8558, Japan
[c] 3D Additive Manufacturing Project Development Group, JEOL Ltd., Akishima, Tokyo 196–8558, Japan

ARTICLE INFO

Associate Editor: Marion Merklein

Keywords:
Powder bed fusion electron beam melting
Thermo-mechanical simulation
Cracking mechanism
Residual stress
TiAl alloy
Non-equilibrium solidification

ABSTRACT

Powder bed fusion electron beam (PBF-EB) melting process with low preheating temperatures is one of the promising ways to fabricate TiAl components with fully lamellar grain satisfying excellent mechanical properties and complex design. In this study, the cracking behavior of a Ti-48Al-2Cr-2Nb alloy produced by electron beam surface melting at 850 °C preheating was investigated under broad building parameter ranges. The transverse crack was more sensitive than the longitudinal crack because of the high tensile strength along the scan direction in single-track melting. The increased crack density deteriorated the tensile strength of the single-track melted Ti-48Al-2Cr-2Nb alloy via interdendritic fracture. Cross-sectional image analysis revealed that the solidification crack was prevented after single-track melting of Ti-48Al-2Cr-2Nb at 850 °C preheating owing to improved liquid feeding, and the crack opening was preferentially observed in the β/B2 phase that was placed near the melt pool boundary region. Based on a Scheil—Gulliver and thermal conduction simulation, the partitioned α and β dendrite regions could be due to the restricted peritectic transformation of $L + \beta \rightarrow \alpha$ during solidification by a rapid cooling rate above 2.3×10^4 °C /s. The crack opening of Ti-48Al-2Cr-2Nb alloy at 850 °C preheating can be suppressed by increasing the line energy above 1.85 J/mm. The critical residual stress causing crack opening in the B2 phase at 1100 °C was determined to be 117 MPa via thermal-elastoplastic analysis. Therefore, cracking due to residual stress of the Ti-48Al-2Cr-2Nb alloy produced by PBF-EB can be predicted as the maximum residual stress in the solidification region.

1. Introduction

In recent decades, a great deal of fundamental developmental research has been conducted on intermetallic compounds for application as high-temperature structural materials (Prasad Rambabu et al., 2017). Titanium-aluminide (TiAl) alloys have attracted considerable attention in the aerospace and automotive industries due to their attractive properties, such as low density, high specific yield strength, high specific stiffness, and superior oxidation resistance at temperatures up to 750 °C (Clemens and Kestler, 2000). The Ti-48Al-2Cr-2Nb (at%) alloy was selected as the GEnx-1B engine component in 2012 as an alternative to the Ni-based superalloy to improve fuel efficiency (>15 %) (Kim and Kim, 2018). However, the major concern about TiAl alloys is their challenging fabrication and complex design due to the inherent brittleness of intermetallic compounds (Kim, 1995). Conventional fabrication processes, such as ingot-metallurgy, investment casting, and thermal mechanical treatment, are inadequate because of the brittle nature and limited formability of TiAl alloys (Tetsui, 2011). Therefore, additive manufacturing has been proposed as a potential candidate for producing TiAl components with near-net-shape and superior properties (Juechter et al., 2018).

During the last decade, there has been extensive research toward producing TiAl components using additive manufacturing techniques. Balla et al. (2016) reported direct energy deposition (DED) of a Ti-48Al-2Cr-2Nb alloy, showing that brittle cracking occurred in broad building parameter ranges due to rapid cooling. Shi et al. (2017) studied the selective laser melting (SLM) of the Ti-47Al-2Cr-2Nb alloy under broad building parameters; however, brittle cracking could not be avoided owing to the large residual stress caused by rapid cooling. Vilaro et al. (2010) pointed out that the brittle cracking of

* Corresponding authors.
E-mail addresses: yim.seungkyun.a3@tohoku.ac.jp (S. Yim), kenta.aoyagi.e7@tohoku.ac.jp (K. Aoyagi), akihiko.chiba.d3@tohoku.ac.jp (A. Chiba).

https://doi.org/10.1016/j.jmatprotec.2023.118104
Received 17 March 2023; Received in revised form 14 July 2023; Accepted 27 July 2023
Available online 29 July 2023

Table 1
Chemical composition of cast Ti-48Al-2Cr-2Nb alloy by ICP analysis.

Sample	Chemical composition (at%)				
	Ti	Al	Cr	Nb	O
Cast Ti-48Al-2Cr-2Nb	48.01	47.90	1.86	2.05	0.19

Ti-47Al-2Cr-2Nb alloys cannot be completely prevented by process parameter optimization of SLM and DED processes, although a second laser source and substrate heating are helpful in preventing brittle cracking. The general principle to alleviate cracking sensitivity is to adopt high-temperature preheating to decrease the cooling rate and residual stress (Li et al., 2016a,b). A dense and crack-free Ti-48Al-2Cr-2Nb alloy was successfully produced via PBF-EB with preheating above 1100 °C (Schwerdtfeger and Körner, 2014). However, long-term preheating at an $\alpha + \gamma$ phase field can result in the segregation of equiaxed γ and thick interlamellar spacing via discontinuous coarsening (DC) (Yim et al., 2021), which decreases the yield and creep strengths above 700 °C (Clemens and Mayer, 2013). Thus, the preheating temperature for building a TiAl alloy should be decreased to further optimize the microstructure and mechanical properties by suppressing the DC reaction during PBF-EB building.

Several studies have attempted to produce TiAl alloys with substrate heating above the ductile-brittle transition temperature (DBTT) using tailored SLM equipment. Caprio et al. (2020) reported that the crack-free Ti-48Al-2Cr-2Nb component is produced by parameter optimization via SLM with preheating at 800 °C. Gussone et al. (2017) demonstrated the crack-free near-lamellar structure of Ti-48Al-2Cr-2Nb alloys using the SLM with preheating at 800 °C. Schimbäck et al. (2021) reported a crack-free fully lamellar microstructure (~20 μm) of Ti-43.5Al-4Nb-1Mo-0.1B via SLM with 900 °C preheating followed by post-heat treatment. Therefore, the additive manufacturing process with preheating above DBTT can replace the conventional process for TiAl alloys with a desirable microstructure and near-net shape. However, Gussone et al. (2015) reported that the brittle cracking of Ti-44.8Al-6Nb-1.0Mo-0.1B alloys cannot be avoided completely even after optimizing the parameters in the SLM process with preheating at 800 and 1000 °C. Although the cracking mechanism of TiAl alloys in the SLM process at low temperatures has been elucidated by Gao et al. (2020a,b), the cracking above DBTT has not been clarified in further detail until now. In contrast, low-temperature preheating in PBF-EB has been mainly limited due to explosive powder scattering by an electrostatic force known as smoke in the preheating process. Chiba et al. (2021) suggested mechanical stimulation to improve the electrical conductivity of Inconel 718 alloy, allowing the raster melting of ball-milled powder without preheating via PBF-EB. Yim et al. (2022a,b) reported that the smoke of a Ti-48Al-2Cr-2Nb alloy is effectively suppressed by mechanical ball milling, and the ball-milled powder does not smoke even when the preheating temperature is lowered to 850 °C. This study clearly demonstrated that TiAl alloys can be produced via PBF-EB at the DBTT temperature without smoke by pretreatment with powder feedstock. Therefore, it is crucial to study the cracking mechanism of Ti-48Al-2Cr-2Nb alloy at DBTT during the PBF-EB process as a primary work.

Consequently, this study aimed to investigate the cracking mechanism of the Ti-48Al-2Cr-2Nb alloy at 850 °C preheating in the PBF-EB building process under various building parameters. Single-track melting was performed to clarify the solidification mechanism of the Ti-48Al-2Cr-2Nb alloy during PBF-EB at 850 °C preheating. The critical factor causing brittle cracking was investigated based on the building parameters. The residual stress threshold causing a crack opening in the Ti-48Al-2Cr-2Nb alloy was approximated using thermal-elastoplastic analysis.

2. Materials and methods

2.1. Sample preparation

The cast Ti-48Al-2Cr-2Nb alloy was prepared by Kobe Steel Ltd., and its chemical composition was analyzed using inductively coupled plasma mass spectrometry (ICP), as shown in Table 1. For homogenization, the as-cast alloy was solution-treated (ST) at 1400 °C (single α phase field) for 1 h in an Ar atmosphere and then furnace-cooled to room temperature (~25 °C) (Fig. 1a). The γ lamellae were precipitated at the α grain matrix during the furnace cooling via diffusional transformation in $\alpha + \gamma$ phase field. The continuous cooling transformation diagram and corresponding microstructure of Ti-48Al-2Cr-2Nb alloy were presented in supplementary data (Fig. S1). The microstructure of the ST alloy consisted of a fully lamellar structure with a mean grain size of 1083 μm and interlamellar spacing of 0.73 μm, as shown in Fig. 1b and c. The fully lamellar grain was selected to examine whether cracks occur in the heat-affected zone or solidification region through single-track melting under low-temperature preheating. Rectangular substrates with dimensions of 15 mm × 15 mm × 2 mm were prepared from the ST alloy using an

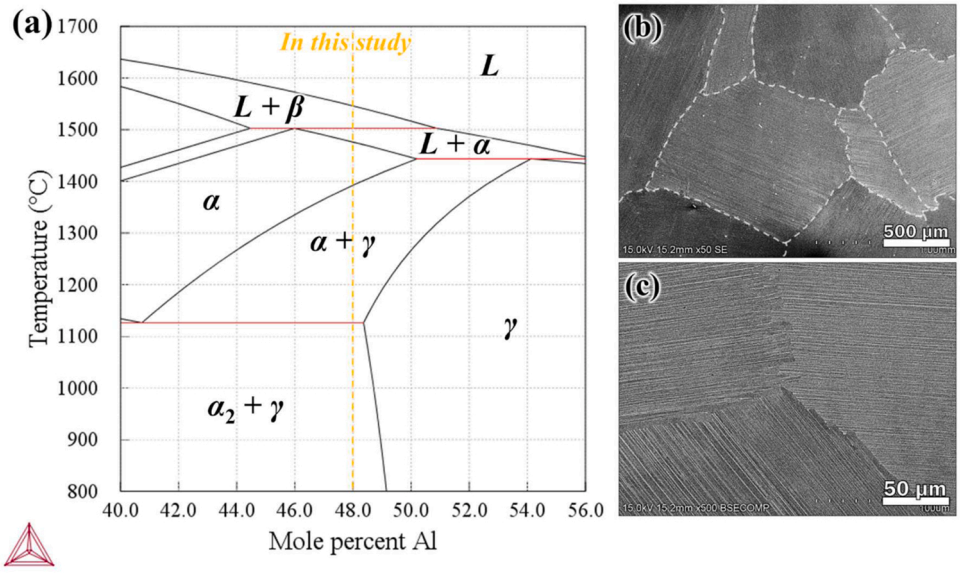

Fig. 1. (a) Binary phase diagram of Ti-Al alloy, microstructure of ST Ti-48Al-2Cr-2Nb alloy at 1400 °C for 1 h; (b) fully lamellar grain, (c) enlarged image.

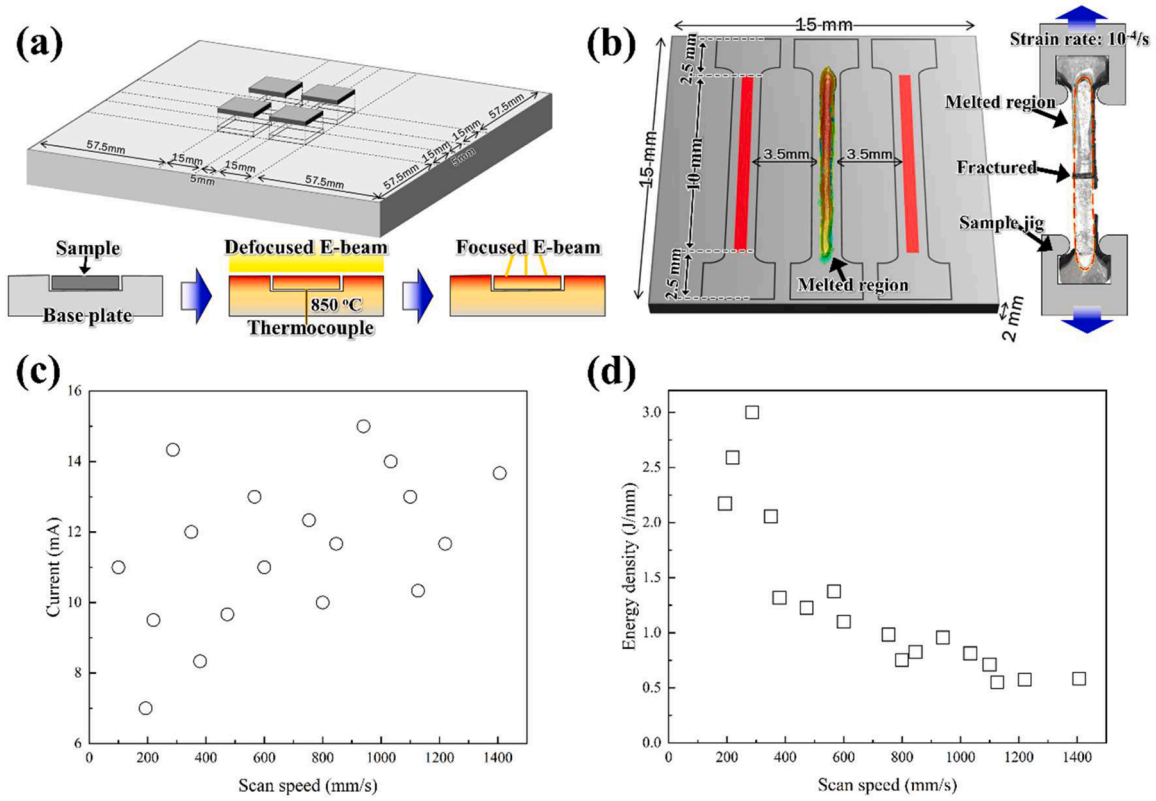

Fig. 2. Schematics of (a) specimen setup and procedure of single-track melting, (b) melt track with tensile specimen. The process parameter for single-track experiment based on (c) current and scan speed, (d) energy density and scan speed.

Table 2
Building parameters and corresponding tensile strength after single-track melting of Ti-48Al-2Cr-2Nb alloys.

Sample	Beam current	Scan speed	Line energy	Tensile strength
S-1	11 mA	100 mm/s	6.60 J/mm	441 MPa
S-2	7 mA	193 mm/s	2.18 J/mm	425 MPa
S-3	9.5 mA	220 mm/s	2.59 J/mm	416 MPa
S-4	14.3 mA	287 mm/s	2.99 J/mm	438 MPa
S-5	12 mA	350 mm/s	2.06 J/mm	437 MPa
S-6	8.3 mA	380 mm/s	1.31 J/mm	413 MPa
S-7	9.6 mA	473 mm/s	1.22 J/mm	411 MPa
S-8	13 mA	567 mm/s	1.38 J/mm	406 MPa
S-9	11 mA	600 mm/s	1.10 J/mm	421 MPa
S-10	12.3 mA	753 mm/s	0.98 J/mm	401 MPa
S-11	10 mA	800 mm/s	0.75 J/mm	367 MPa
S-12	11.6 mA	847 mm/s	0.82 J/mm	214 MPa
S-13	15 mA	940 mm/s	0.96 J/mm	301 MPa
S-14	14 mA	1033 mm/s	0.81 J/mm	282 MPa
S-15	13 mA	1100 mm/s	0.71 J/mm	267 MPa
S-16	10.3 mA	1127 mm/s	0.55 J/mm	284 MPa
S-17	11.6 mA	1220 mm/s	0.57 J/mm	316 MPa
S-18	13.6 mA	1407 mm/s	0.58 J/mm	255 MPa
S-t	11 mA	357 mm/s	1.85 J/mm	-

electro-discharge machine, and mechanically ground using SiC grade #2400 paper.

2.2. Single-track melting experiment

Single-track melting experiments with electron beams were conducted using JEOL electron beam metal AM equipment (JBS-Z0100EBM, JEOL Ltd., Japan). The machined base plate at the center was dug into four square holes with dimensions 15 mm × 15 mm × 3 mm (Fig. 2a). The ST substrates were placed in machined holes, and the base plate was preheated to 850 °C (above the DBTT) using a defocused electron beam under a vacuum atmosphere ($<10^{-3}$ Pa). After heating for 5 min at 850 °C, single-track melting was conducted using various building parameter sets with three lines, as shown in Fig. 2b. The broad range of beam current and scan speed was determined via a uniform design method, one of the designs of experimental techniques (Fang et al., 2000), as shown in Table 2. The line energy density (E_L) of an electron beam can be defined as follows:

$$E_L = \frac{V \times I}{v} \quad (1)$$

where V is the acceleration voltage of 60 kV, I is the electron beam current, and v is the scan speed. The over or under-estimated parameters that cause severe or weak melting were manually changed to the interest range, as shown in Fig. 2c and d.

2.3. Microstructure observation

The crack occurrence of Ti-48Al-2Cr-2Nb substrates after single-track melting was examined by observing the melted surface and cross-sectional microstructures. The single-track melted sample was cut into five sections using an electro-discharge machine and then mechanically ground using SiC paper to remove oxide layers and polished using the op-s solution. The polished samples were etched using the Kroll's Titanium Etch (4 vol% HNO_3, 6 vol% HF, 23 vol% H_2O_2, and 67 vol% H_2O). The microstructure of single-track melted sample was observed using field emission scanning electron microscopy (SEM, JSM-IT800, JEOL Ltd., Japan). The surface and cross-sectional images of single-track melted samples using the parameter sets are presented in supplementary data (Figs. S2 and S3). The element distribution in melt pool region was examined using the field emission electron probe micro analyzer (EPMA, JXA-8530F, JEOL Ltd., Japan). The crack density was defined as the total crack length in the melt pool area using the surface and cross-sectional images. In the single-track melting experiment, the

Table 3
Numerical parameters for the finite element simulation of Ti-48Al-2Cr-2Nb alloy.

Parameter	Value	Unit
Acceleration voltage	60	kV
Beam current	7–14.3	mA
Scan speed	100–1407	mm/s
Beam absorption coefficient	0.814	
Beam diameter	0.5–0.75	mm
Emissivity	0.36	
Chamber temperature	25	°C
Preheating temperature	850	°C
Solidus	1461	°C
Liquidus	1552	°C
Stress reset temperature	1552	°C

melt pool tail that finally solidified region contained brittle cracking due to rapid cooling. Therefore, the sample containing only tail edge cracking was considered crack-free. The dog-bone-shaped specimens for the tensile test were prepared using the single-track melted alloy for fractography analysis, as shown in Fig. 2b. In the tensile specimen, the head and neck regions were non-melted with a dimension of 3.5 mm × 2.5 mm, while the central region contained the melted line by single-track electron beam melting with a dimension of 1.5 mm × 10 mm. The tensile test was performed using a specially designed jig for a single-track melting specimen with a strain rate of 10^{-4}/s at room using the Instron tensile system at a load of 250 kg under room temperature following ASTM D638. The measured tensile strengths of single-track melted samples showed a high discrepancy depending on the building parameter sets. The tensile strength of single-track melted samples was increased with line energy despite increased melting region. Thus, it was considered that the difference in tensile strength was mainly due to the crack density caused by the single-track melting via PBF-EB.

2.4. Thermal-elastoplastic analysis

The 3D thermal conduction model was developed using a commercial Abaqus finite element code to compute the temperature fields during single-track melting of the Ti-48Al-2Cr-2Nb substrate. The heat conduction during single-track melting at each time-step level was defined using the energy conservation equation:

$$\rho C_p \frac{\partial T}{\partial t} = k\left(\frac{\partial^2 T}{\partial x^2} + \frac{\partial^2 T}{\partial y^2} + \frac{\partial^2 T}{\partial z^2}\right) + Q \tag{2}$$

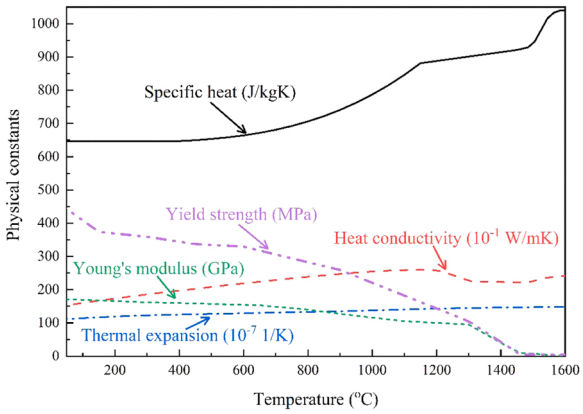

Fig. 4. Temperature-dependent material properties of the Ti-48Al-2Cr-2Nb alloy.

where ρ is the density, C_p is the specific heat, κ is the thermal conductivity of the materials, x, y, z, are the Cartesian coordinates, and Q is the rate of heat per unit of volume. The radiation heat loss on the single-track melted surface can be defined using the Stefan–Boltzmann law:

$$q_{rad} = \varepsilon\sigma\left(T_s^4 - T_v^4\right) \tag{3}$$

where ε is the emissivity coefficient, σ is the Stefan–Boltzmann constant, T_s is the surface temperature, and T_v is the temperature of the vacuum chamber. The convective heat loss was neglected because of the vacuum conditions of the PBF-EB process. A user-defined Fortran program was developed to model the electron beam heat source. The heat flux distribution of the electron beam is approximated as a Gaussian distribution as follows:

$$q(r) = \frac{\eta VI}{2\pi r_0^2}\exp\left(-\frac{r^2}{2r_0^2}\right) \tag{4}$$

where η is the absorption efficiency of the electron beam, r_0 is the beam diameter, and r is the distance from the center of the heat source. From the thermal conduction model, the cooling rate in the melt pool can be approximated as follows:

$$\frac{\partial T}{\partial t} = \left|\frac{T_L - T_S}{t_L - t_s}\right| \tag{5}$$

where T_L is the liquidus temperature, T_S solidus temperature, and t_L and

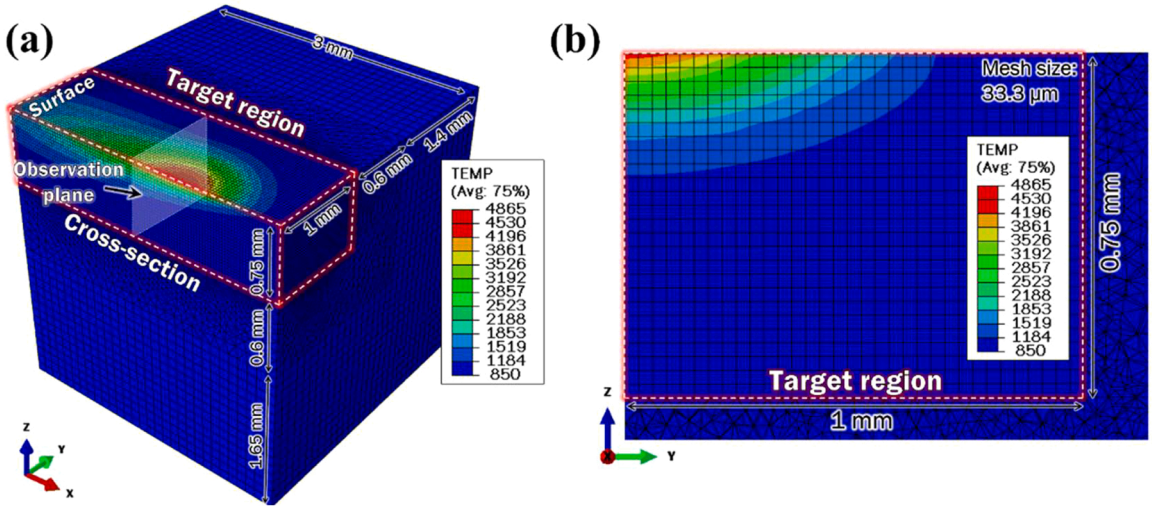

Fig. 3. Finite element model for single-track melting of Ti-48Al-2Cr-2Nb alloy; (a) 3d model, (b) cross-section of target region (observation plane).

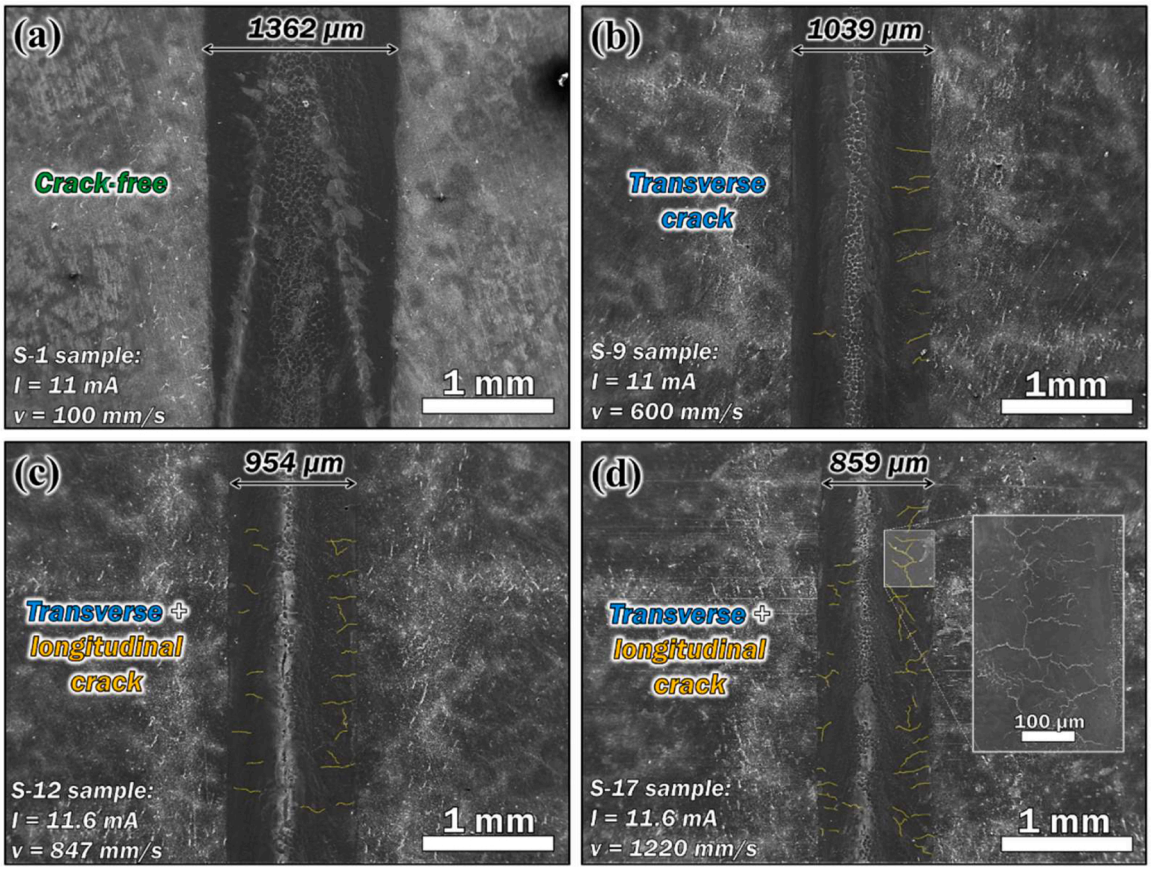

Fig. 5. Surface image of single-track melted Ti-48Al-2Cr-2Nb alloy under various building parameters; (a) S-1 (*I*: 11 mA, *v*: 100 mm/s), (b) S-9 (*I*: 11 mA, *v*: 600 mm/s), (c) S-12 (*I*: 11.6 mA, *v*: 847 mm/s), (d) S-17 (*I*: 11.6 mA, *v*: 1220 mm/s).

t_S are the times that reach the liquidus and solidus temperatures, respectively. The numerical parameters for the thermal conduction model are listed in Table 3. The constructed thermal conduction model is shown in Fig. 3a and b. The target region was set to a fine mesh (33.3 μm), and the electron beam was moved along the x-direction in the model edge to decrease the computational cost. The initial temperature

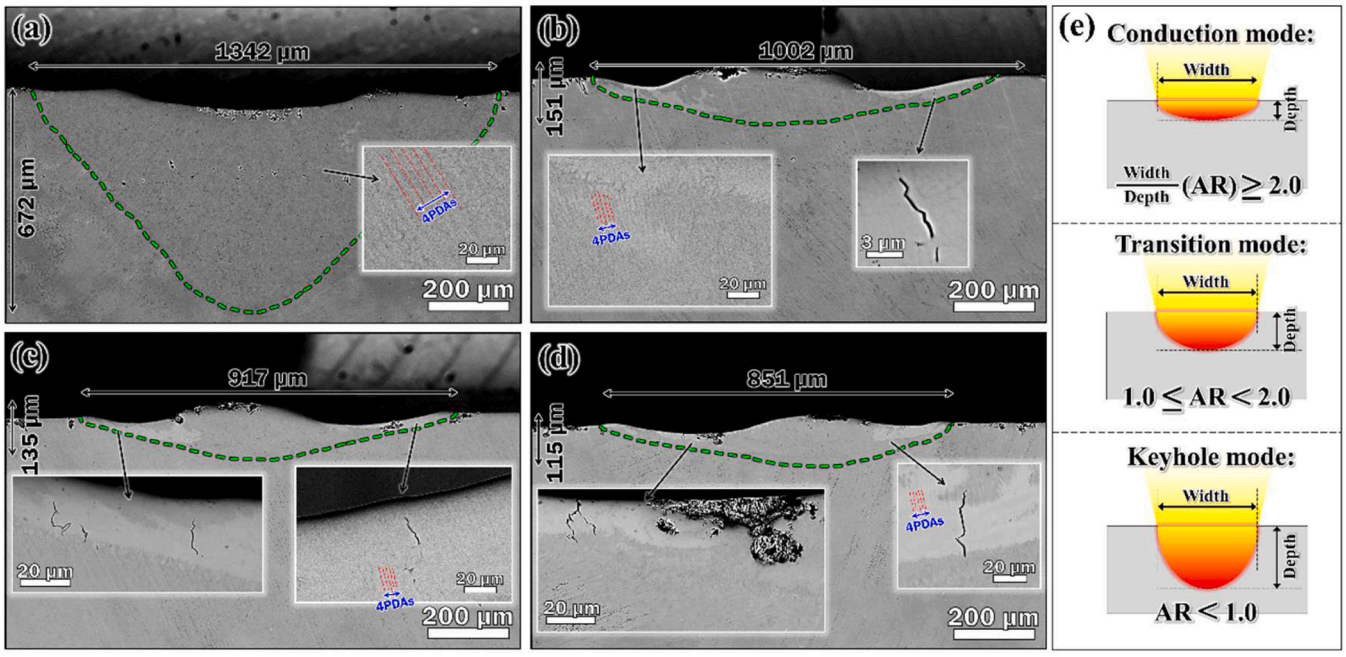

Fig. 6. Cross-sectional BSE image of single-track melted Ti-48Al-2Cr-2Nb alloy; (a) S-1 (*I*: 11 mA, *v*: 100 mm/s), (b) S-9 (*I*: 11 mA, *v*: 600 mm/s), (c) S-12 (*I*: 11.6 mA, *v*: 847 mm/s), (d) S-17 (*I*: 11.6 mA, *v*: 1220 mm/s); (e) schematic of melt pool classification depending on the aspect ratio.

Table 4
Mean primary dendrite arm spacing of single-track melted Ti-48Al-2Cr-2Nb alloys.

	S-1	S-9	S-12	S-17
Mean primary dendrite arm spacing	5.63 μm	2.21 μm	2.04 μm	1.87 μm

of the constructed model was set to 850 °C, and the boundaries, except for the surface and cross-section, were set to adiabatic conditions. The temperature-dependent material properties of the Ti-48Al-2Cr-2Nb alloy were taken from the literature and Scheil simulations using ProCAST software (Yan et al., 2016) and are presented in Fig. 4. The absorption coefficient of electron beam was determined using the calculation of backscattering coefficients via a Monte Carlo simulation based on mean energy loss model (Yim et al., 2022a,b). In the thermal-elastoplastic analysis, the von Mises yield criterion was employed to calculate the thermally induced stress and strain, which were reset to zero at temperatures above the liquidus to approximate the residual stress after solidification.

3. Results

3.1. Microstructure of single-track melted alloy

The surface images of single-track melted Ti-48Al-2Cr-2Nb alloys depending on the building parameters are presented in Fig. 5a—d. A crack-free surface was observed in the S-1 sample at a beam current of 11 mA and scan speed of 100 mm/s, while a transverse crack with a length below 500 μm was detected in the S-9 sample as the scan speed increased to 600 mm/s (Fig. 5a and b). This transverse crack was focused on the edge region of the melt track and could be attributed to the supplied tensile stress along the scan direction of the electron beam. In the S-12 and S-17 samples, the crack length and density further increased with scan speed despite the slightly increased beam current, and longitudinal cracks were observed at scan speeds above 847 mm/s (Fig. 5c and d). This result indicates that the transverse crack more favorably occurs during the solidification process than the longitudinal crack, and the tendency of cracking increases with increasing scan speed.

The cross-sectional BSE images of single-track melted Ti-48Al-2Cr-2Nb substrates, depending on the building parameters, are presented in Fig. 6a—d. The melt pool geometries were determined based on the aspect ratio (AR) of the melt pool width to the depth: conduction (AR $\geq$ 2.0), transition (1.0 $\leq$ AR $<$ 2.0), and keyhole (AR $<$ 1.0) modes. The high energy input can cause severe metal vaporization and residual cavities in the key-hole mode, while the low energy input can suppress metal vaporization and internal defects by the rapid heat dissipation in the conduction mode (Wei et al., 2017). The AR of the S-1 sample was $<$ 2.0, indicating the transition mode, while the others were $>$ 2.0, indicating the conduction mode. In single-track melted samples, the dendritic-cellular microstructure can be separated into three contrast colors in backscattered electron imaging: bright gray, middle gray, and dark gray regions due to different element compositions (Fig. 6a—d). The microstructure of the S-1 sample mainly consisted of middle gray columnar dendritic and dark gray interdendritic regions, and the circular pores were observed at the center region of the melt pool. Zhao et al. (2020) reported that the high recoil pressure caused by the metal vaporization resulted in melt pool depression with intense heat convection (i.e. Marangoni and buoyancy flows) and facilitates pore formation. Thus, the formation of residual pores could be activated in the transition mode in the PBF-EB process of TiAl alloy. As the heat transfer mode changed to the conduction mode, the fraction of the bright gray region increased near the melt pool surface or boundary (colored by a green dashed line), and the crack opening was preferentially started in the bright gray region, as shown in Fig. 6b—d. It is well known that the residual pores act as a precursor to fracture initiation under tensile stress by decreasing final fracture stress (Yim et al., 2021). This result suggests that the residual pores in the solidified region were not a major factor to cause the cracking of TiAl alloy in the PBF-EB process with 850 °C preheating. The mean primary dendrite arm spacing (PDAS) of the S-1 sample was 5.63 μm, and it gradually decreased with increasing scan speed, as shown in Table 4. It has been reported that PDAS (λ_1) is

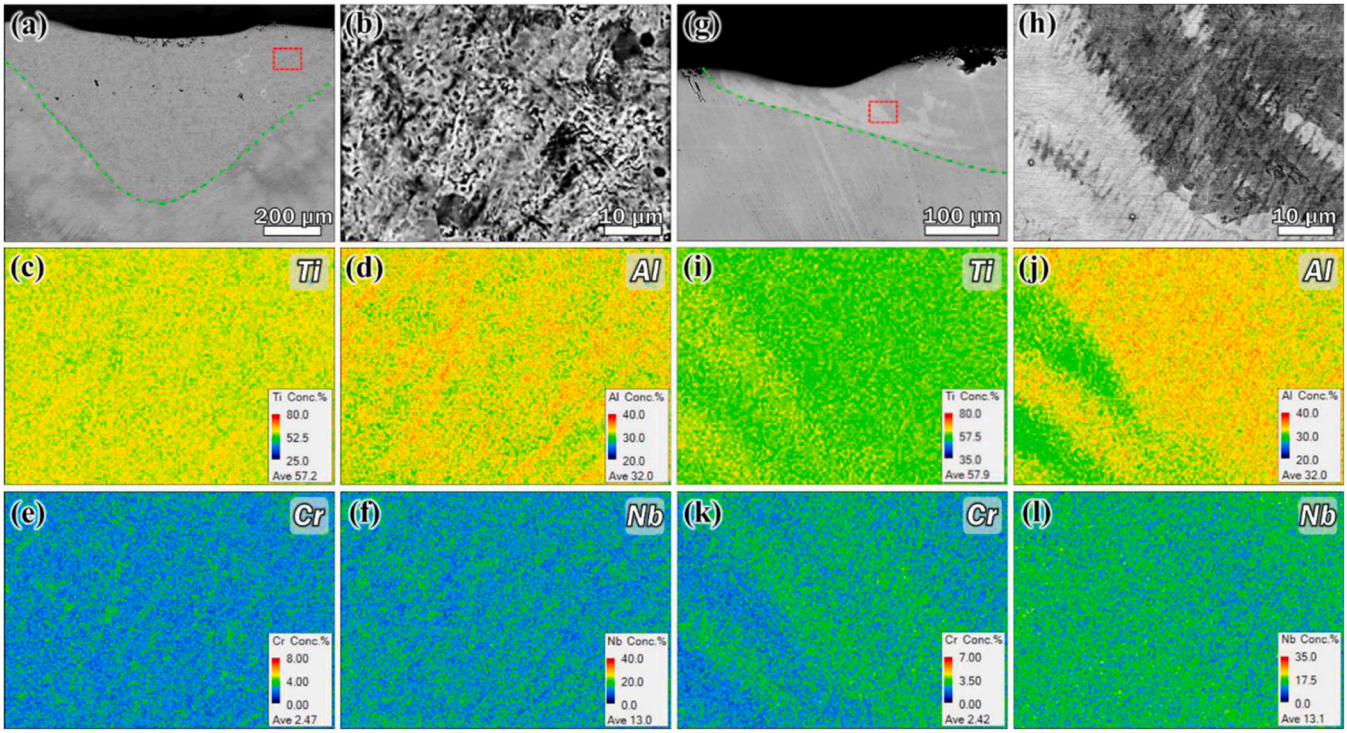

Fig. 7. Cross-sectional BSE and EPMA element mapping image of single-track melted Ti-48Al-2Cr-2Nb alloy; (a)—(f) S-1, (g)—(l) S-9 samples.

Table 5
Atomic concentration of phases in S-1 and S-9 samples by EPMA analysis.

Sample	Phase	Atomic concentration (at%)			
		Ti	Al	Cr	Nb
S-1	β/B2	53.68	39.77	1.12	5.43
	α_2	49.75	43.77	2.11	4.37
	γ	44.81	50.25	3.17	1.77
S-9	β/B2	55.15	38.35	0.41	6.08
	α_2	49.66	44.11	1.63	4.59
	γ	45.33	49.31	3.35	2.01

inversely proportional to the cooling rate (Liu et al., 2016):

$$\lambda_1 = A \bullet \left(\frac{\partial T}{\partial t}\right)^n \quad (6)$$

where A is a constant that is mainly related to the solidification characteristic of the alloy, and n is the rate exponent (−0.31). Based on the PDAS, the cooling rate of the S-9 sample was approximately 20 times higher than that of the S-1 sample, and this difference was increased to 26 and 30 times in the S-12 and S-17 samples, respectively. This result indicates that the cooling rate of the conduction mode is much higher than that of the transition mode owing to the low line energy, and crack opening is favored in the conduction mode due to the high tensile force produced by rapid cooling.

To examine the phases of solidified Ti-48Al-2Cr-2Nb alloys after single-track melting, EPMA element mapping analysis was performed. The BSE and element mapping images of the S-1 and S-9 samples are presented in Fig. 7a—l. The solidification region of single-track melted samples consisted of three phases depending on the chemical composition: β/B2 phase (bright gray), α_2-Ti_3Al (middle gray), and γ-TiAl (dark gray), as shown in Table 5. In the S-1 sample, Nb was distributed in β/B2 and α_2-Ti_3Al phases, while Cr was mainly concentrated in the γ-TiAl phase, as shown in Fig. 7e and f. In contrast, a partitioned microstructure was observed in the S-9 sample, which was classified into bright and middle gray columnar dendritic regions. In the S-9 sample, Nb was homogeneously distributed in the bright and middle gray columnar dendritic regions, while the Al and Cr elements were depleted in the bright gray region, as shown in Fig. 7j and k. This result indicates that the solidification path of Ti-48Al-2Cr-2Nb can be changed depending on the building parameters of PBF-EB.

3.2. Fractography analysis of single-track melted alloy

The cross-sectional fracture surfaces of the single-track melted samples are presented in Fig. 8a—d. In the TiAl alloy, which consisted of lamellar grains, the crack propagated along the lamellar interface or passed through the α_2/γ lamellae. Interlamellar and translamellar-like fracture morphologies were observed in the melt pool region of the S-1 and S-9 samples with high tensile strength (>400 MPa), as shown in Table 2. However, interdendritic fracture morphologies were observed (red arrow in Fig. 8c and d) in the S-12 and S-17 samples, respectively, and their tensile strengths decreased to < 316 MPa. The interdendritic fracture region was near the melt pool surface or boundary, which was comparable to the β/B2 phase region. This result suggests that precracking in the β/B2 phase region could significantly decrease the tensile strength of the single-track melted Ti-48Al-2Cr-2Nb alloy via interdendritic fracture.

The classification of brittle cracking and the measured crack density after single-track melting are presented in Fig. 9a and b. The single-track melted sample that contained only an edge crack at the end of the single-track was considered crack-free because it had minor effects on the tensile strength. The crack density in the melt pool region rapidly decreased depending on the line energy up to 1.32 J/mm, and it evolved to crack-free above 2.06 J/mm. This result suggests that the crack density in single-track melted Ti-48Al-2Cr-2Nb alloy could be predominantly affected by the increase of line energy than the manipulating

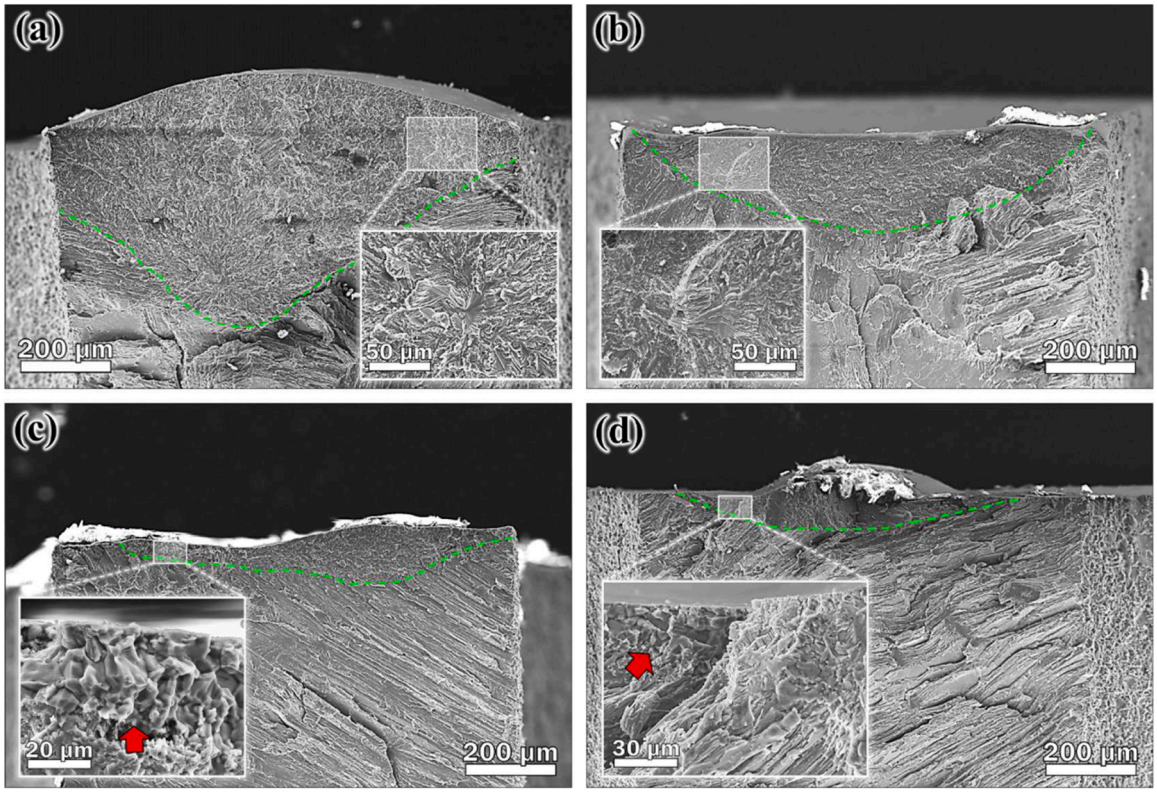

Fig. 8. Fracture surface image of single-track melted Ti-48Al-2Cr-2Nb alloy; (a) S-1 (*I*: 11 mA, *v*: 100 mm/s), (b) S-9 (*I*: 11 mA, *v*: 600 mm/s), (c) S-12 (*I*: 11.6 mA, *v*: 847 mm/s), (d) S-17 (*I*: 11.6 mA, *v*: 1220 mm/s). (Red arrow indicates the interdendritic fracture region).

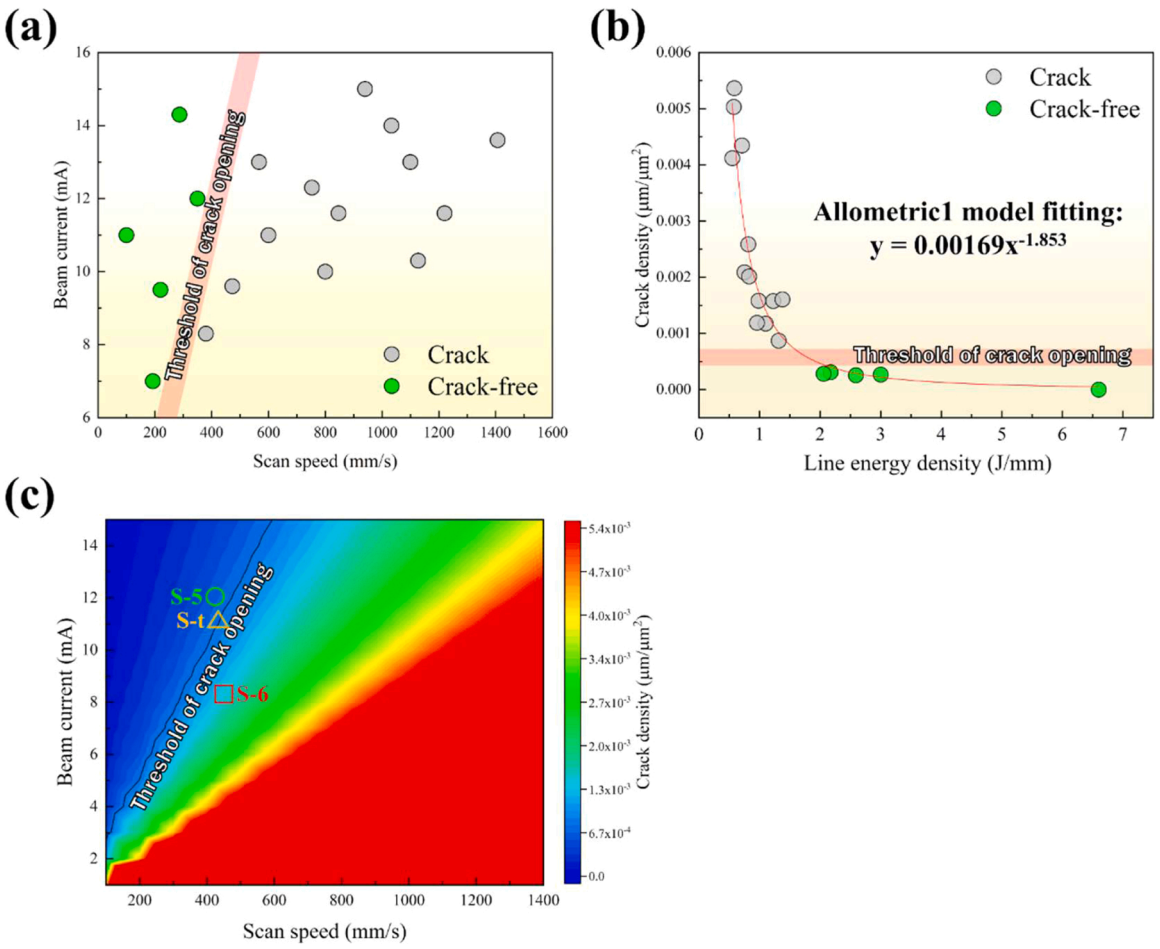

Fig. 9. (a) Classification chart of brittle cracking, (b) crack density, (c) predicted process parameter map with crack density. (S-t indicates the manually selected threshold point of the crack opening).

current and scan speed at low line energy. A clear allometric relation between the crack and line energy densities was identified. Based on the line model fitting, the threshold of the crack opening according to the building parameters was predicted, as shown in Fig. 9c. This classification chart suggests that the crack opening of the Ti-48Al-2Cr-2Nb alloy in single-track melting via PBF-EB at 850 °C preheating would be restricted at a line energy above 1.85 J/mm by manipulating scan speed and beam current.

3.3. Thermal conduction model validation

To understand the solidification and cracking mechanisms of the Ti-48Al-2Cr-2Nb alloy in the single-track melting process, thermal-elastoplastic analysis was conducted using various building parameters. It is well known that the absorption coefficient of the electron beam was much higher compared to that of the laser beam (Körner, 2016). On the other hand, the melt pool diameter was significantly altered depending on the building parameters despite the fixed beam diameter and focus offset owing to the instability of the electron beam. Thus, the melt pool geometry depending on the building parameters in the simulation was calibrated using the beam diameter of the electron beam under a fixed absorption coefficient. The calculated temperature distribution by the thermal conduction model, depending on the building parameters, is presented in Fig. 10a—d. The thermal conduction model was calibrated based on the melt pool geometries and sizes of the single-track melted samples. The pseudo-full model was produced by inverting one side image using a mirror function, and the temperature above the liquidus (1552 °C) was represented as gray-colored to compare the shape and size of the melt pool with the experimental result. The simulated melt pool width and depth of the S-1 sample were not accurately matched to the experimentally measured results, while its magnitude was roughly matched, as shown in Fig. 10a. Zhao et al. (2020) reported that melt pool geometry was mainly affected by vapor recoil pressure as increasing energy input in the PBF-AM process. Lei et al. (2022) demonstrated that the melt pool width was decreased without the effect of fluid flow (i.e. Marangoni and buoyancy convections) transferring thermal energy from the melt pool center to the outer, while the temperature distribution in the melt pool was similar. Thus, the discrepancy between the simulation and experiment of the S-1 sample might be originated from neglected recoil pressure and molten pool flow. In the other building parameter conditions, the geometry and magnitude of the melted area that was heated above the liquidus temperature were also roughly matched. Thus, the melt pool flow in the simulation can be neglected because of the similar temperature distributions in the melt pool, which cause a similar residual stress degree.

3.4. Solidification behavior of the Ti-48Al-2Cr-2Nb alloy

The cooling rate obtained by the thermal conduction model during solidification of the Ti-48Al-2Cr-2Nb alloy depending on the building parameters is presented in Fig. 11a—d. The maximum cooling rate of the S-1 sample was lower than that of S-9 almost 1/23 times, and it gradually increased in the S-12 and S-17 samples as the scan speed increased, which was well matched to the cooling rate difference according to building parameters based on PDAS. The cooling rate in all samples was the most rapid near the melt pool boundary or edge of the surface

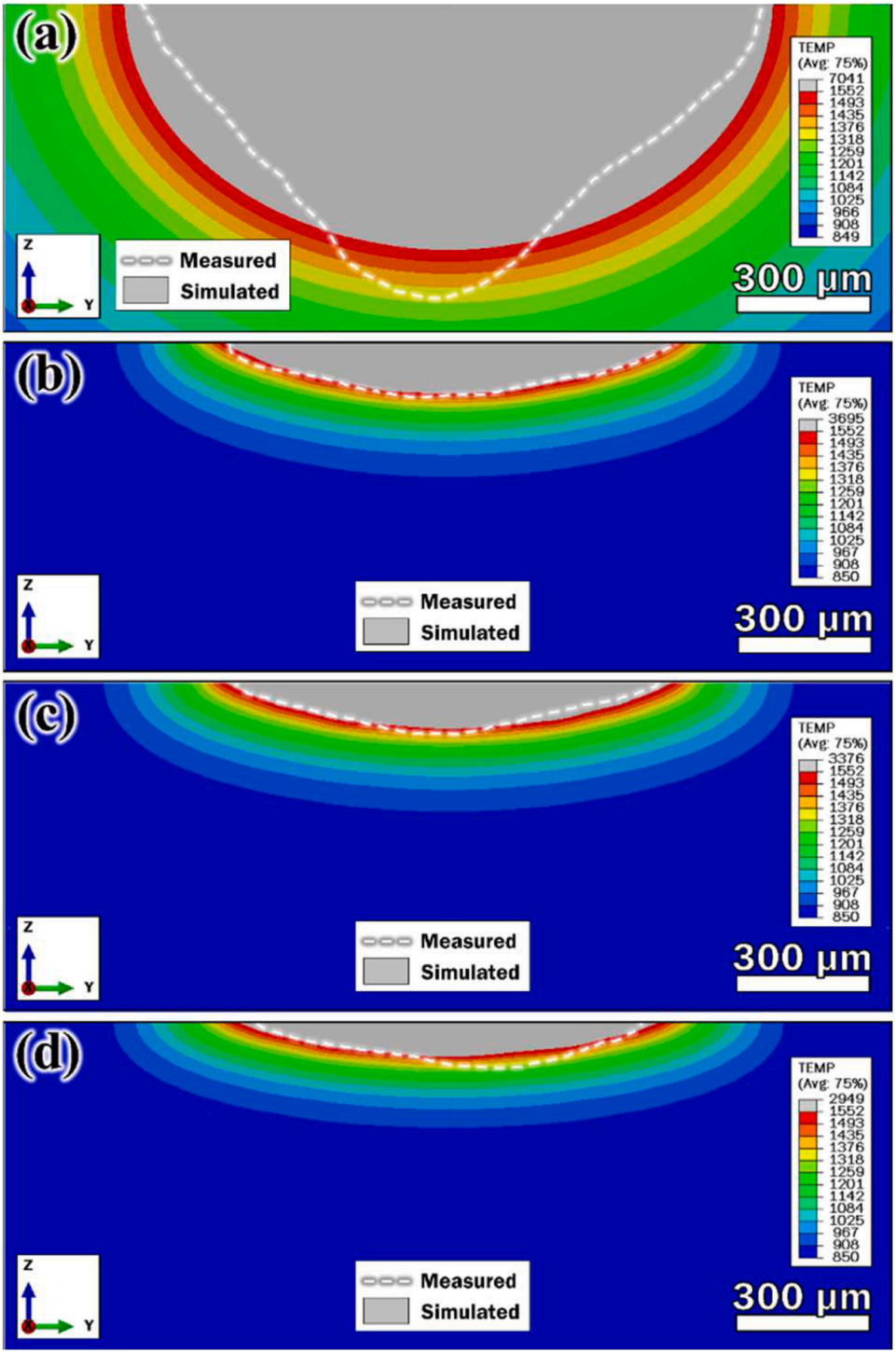

Fig. 10. Snapshot image of the thermal conduction model with temperature distribution; (a) S-1 (*I*: 11 mA, *v*: 100 mm/s), (b) S-9 (*I*: 11 mA, *v*: 600 mm/s), (c) S-12 (*I*: 11.6 mA, *v*: 847 mm/s), (d) S-17 (*I*: 11.6 mA, *v*: 1220 mm/s). (The white dotted line indicates the experimentally measured melt pool area).

because of rapid heat dissipation via thermal conduction and radiation, whereas it was relatively slow in the melt pool center. This result implies that the temperature gradient of solid/liquid interface could be higher at the melt pool boundary or edge of the surface than that in the melt pool center. The high cooling rate regions in the S-9, S-12, and S-17 samples were comparable to the β/B2 phase region, as shown in Fig. 11b—d.

In the non-equilibrium solidification process, the dendritic microstructure is determined by the temperature gradient (G) and solidification rate (R) at the solid/liquid interface. From the thermal conduction model, the temperature gradient can be determined using Fourier's law, as follows:

$$G = \frac{|\vec{q}|}{k} = \sqrt{G_x^2 + G_y^2 + G_z^2} \tag{7}$$

where $|\vec{q}|$ is the magnitude of the heat flux vector, and k is the thermal conductivity at the T_L (1552 °C). The solidification rate, R, which is the moving velocity of the solid–liquid interface, can be calculated by

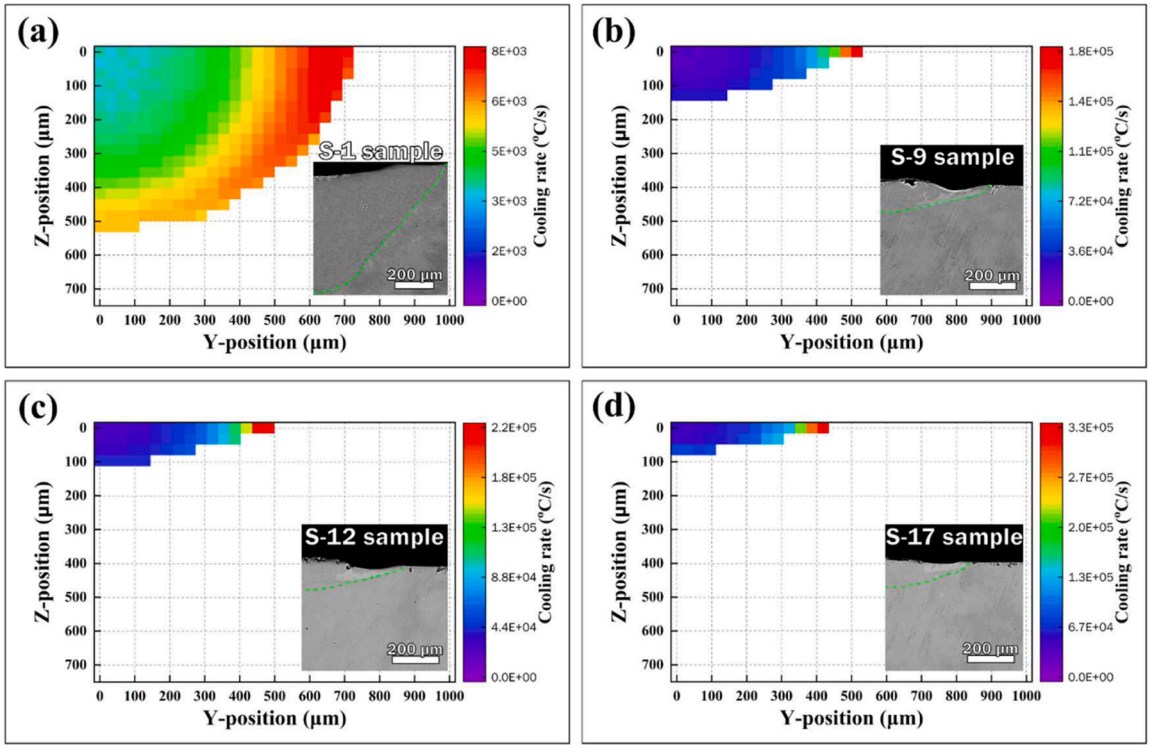

Fig. 11. Cooling rate distribution during solidification of Ti-48Al-2Cr-2Nb alloy; (a) S-1 (*I*: 11 mA, *v*: 100 mm/s), (b) S-9 (*I*: 11 mA, *v*: 600 mm/s), (c) S-12 (*I*: 11.6 mA, *v*: 847 mm/s), (d) S-17 (*I*: 11.6 mA, *v*: 1220 mm/s). (The green dotted line indicates the melt pool boundary).

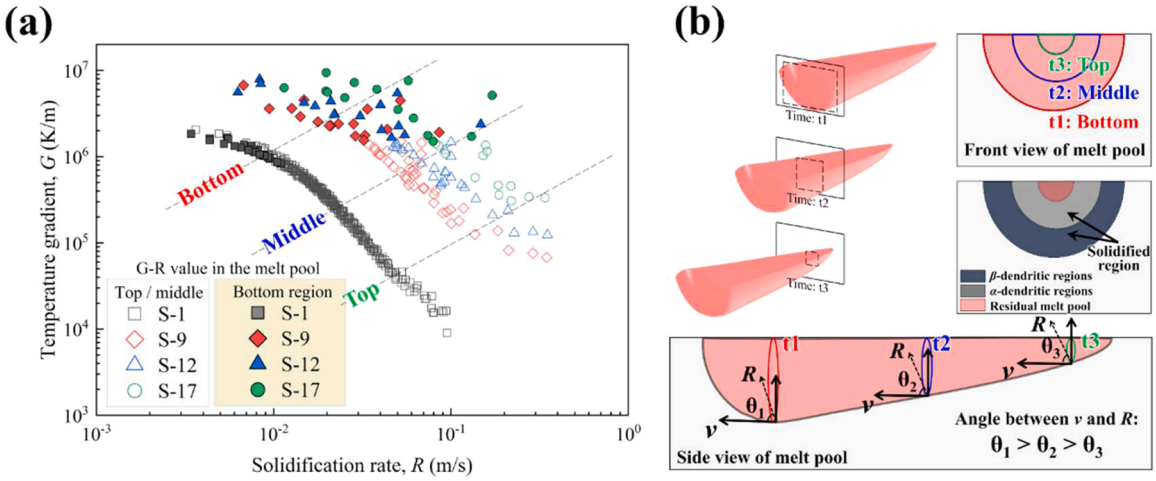

Fig. 12. (a) *G* and *R* distribution during solidification of Ti-48Al-2Cr-2Nb alloy depending on building parameters, (b) angle between the direction of *v* and *R*, solidified microstructure depending on melt pool position.

$$R = v \bullet \cos\theta = v \bullet \left|\frac{G_x}{G}\right| \tag{8}$$

where θ is the angle between the direction of the electron beam scan speed (v) and R. The G and R values in the single-track melting of the Ti-48Al-2Cr-2Nb alloy under various building parameters were measured at the observation plane of center part, as shown in Fig. 3a. The G and R distributions at the observation plane during the solidification of the Ti-48Al-2Cr-2Nb alloy depending on the building parameters are presented in Fig. 12a. In all samples, the solidification velocities at the bottom region of melt pool were lower than those at the middle and top areas, while the temperature gradient was higher. This result indicates that the angle between v and R was highest in the bottom region of the melt pool, while it gradually decreased in the middle and top regions, causing high solidification velocity (Fig. 12b). In the interface response function theory, the influence of solidification rate on the temperature of the solidified interface is reflected at a given composition and temperature gradient (Su et al., 2005). Thus, the primary solidified phase is dominantly affected by the G/R ratio, which represents the undercooling of the solid–liquid interface. The constitutional undercooling (ΔT_c) in the dendrite tip can be expressed as (Gäumann et al., 1997)

$$\Delta T_c = GD_L/R \tag{9}$$

where D_L is the diffusion coefficient of the solute in liquid (5×10^{-9} $m^2 \cdot s^{-1}$). The mean ΔT_c in the melt pool bottom area was higher than that in the melt pool top and middle regions in all samples, and it gradually

Table 6
Constitutional under cooling in the melt pool bottom region of single-track melted Ti-48Al-2Cr-2Nb alloys.

	S-1	S-9	S-12	S-17
Constitutional under cooling	0.83 °C	0.53 °C	0.48 °C	0.44 °C

decreased with increasing scan speed. However, the mean ΔT_c in the melt pool bottom was < 1 °C in all samples (Table 6). Su et al. (2005) reported that the primary phase of Ti-48Al alloy can vary depending on the G/R ratio, and the primary dendrite β is more favored under low undercooling than primary dendrite α. Graf et al. (2021) demonstrated using in situ high-energy X-ray diffraction that the β phase is the primary dendrite phase in the solidification of Ti-48Al-2Cr-2Nb alloy by SLM. This result indicates that the β phase could be the primary dendrite in all samples after single-track melting at preheating temperature of 850 °C owing to the low ΔT_c. Thus, the primary β phase will grow larger until the nucleation undercooling of the α phase is achieved (Zhu et al., 2012). Therefore, the solidification and solid-state transformation of the Ti-48Al-2Cr-2Nb alloy during the single-track melting can be expressed as (Li et al., 2016a,b)

$$L \rightarrow L+\beta \rightarrow \beta+\alpha \rightarrow \alpha+\gamma+\beta \rightarrow \alpha_2+\gamma+B2 \quad (10)$$

However, the magnitude of the β dendritic region was clearly different depending on the building parameters. Liu et al. (2015a), reported that β is the primary phase at high undercooling levels caused by rapid cooling, and the peritectic transformation of $L+\beta \rightarrow \alpha$ in the Ti-48Al-2Cr-2Nb alloy can be restrained at a cooling rate of 2.3×10^4 °C /s. This result suggests that $L+\beta \rightarrow \alpha$ is favored at a low cooling rate (< 2.3×10^4 °C /s), and it allows the superposition of multiple-phase transformation reactions during solidification. Thus, the $\beta+\alpha+\gamma$ mixed dendritic microstructure of the S-1 sample could attribute to the peritectic transformation during solidification under a low cooling rate, as shown in Fig. 7b. In contrast, the peritectic transformation in S-9 sample could be restricted due to the rapid cooling rate (> 2.3×10^4 °C /s), which restricts the diffusion of elements during solidification. Therefore, the β dendritic region containing almost no α phase can be obtained in the S-9, S-12, and S-17 samples near the melt pool boundary region due to the suppressed peritectic $L+\beta \rightarrow \alpha$ reaction by rapid cooling.

To further examine the solidification behavior of the Ti-48Al-2Cr-2Nb alloy, a Scheil—Gulliver simulation was conducted using the Thermo-Calc software with the TTTI3 v3.1 database. The solidification behavior and corresponding element concentration in the liquid of Ti-48Al-2Cr-2Nb alloy are presented in Fig. 13a and b. Under the Scheil—Gulliver condition, the solidification path of the Ti-48Al-2Cr-2Nb alloy is as follows:

$$L \rightarrow L+\beta \rightarrow L+\beta+\alpha \rightarrow L+\alpha \rightarrow L+\alpha+\gamma \rightarrow L+\gamma \rightarrow L+\gamma+\beta \quad (11)$$

The primary solidified phase was β-depleted of Al and Cr at temperatures up to 1484 °C, as shown in Fig. 13a. The Al and Cr concentrations in the liquid gradually increased during solidification (Fig. 13b) due to the low partition coefficients of Al and Cr (Table 7). This result suggests that the β-dendritic regions in the S-9, S-12, and S-17 samples could be primarily formed by rapid solidification near the melt pool bottom region, and the α-dendrite region is subsequently formed in the top or middle regions due to the increased Al and Cr concentrations in the liquid, as shown in Fig. 12b.

3.5. Cracking mechanism of Ti-48Al-2Cr-2Nb alloy

In this study, thermally-induced brittle cracking was only observed after single-track melting of the Ti-48Al-2Cr-2Nb alloy. Lee et al. (2020) reported that the solidification crack near the centerline is the dominant cracking behavior of the Ti-48Al-2Cr-2Nb alloy in the SLM process without preheating. Gao et al. (2020a,b) reported that solidification cracking in the central region of Ti-40Al-9V-0.5Y mainly occurred with increasing scan speeds during the SLM process without preheating. It is well known that solidification cracking is occurred at the final shrinkage region by the contribution of lack of liquid feeding and residual stress above solidus temperature, while cold cracking occurs below solidus temperature owing to the accumulation of thermal stress (Deng et al., 2022). In this study, solidification cracking in the Ti-48Al-2Cr-2Nb alloy was prevented under a broad building parameter range (even in the transition mode) via PBF-EB with preheating at 850 °C. This result indicates that preheating at 850 °C can contribute to liquid feeding as well as residual stress release during solidification after single-track melting. Zhao et al. (2019) reported that heat transfer in the melt pool is predominantly affected by heat convection rather than heat conduction under low viscosity due to Marangoni convection. The dynamic viscosity of the liquid in the melt pool can be expressed as (Nie et al., 2018):

Table 7
Partition coefficient of Ti-48Al-2Cr-2Nb alloy under Scheil—Gulliver conditions at 1450 °C.

	Ti	Al	Cr	Nb
Partition coefficient	1.103	0.872	0.399	1.199

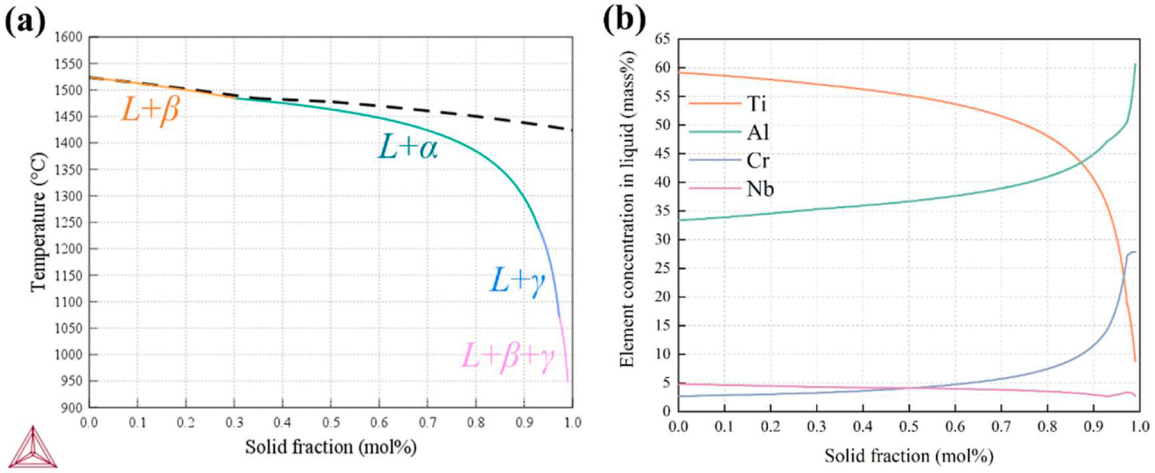

Fig. 13. (a) Scheil—Gulliver simulation and (b) corresponding element concentration of Ti-48Al-2Cr-2Nb alloy during solidification. (Black dotted line indicates the equilibrium solidification condition).

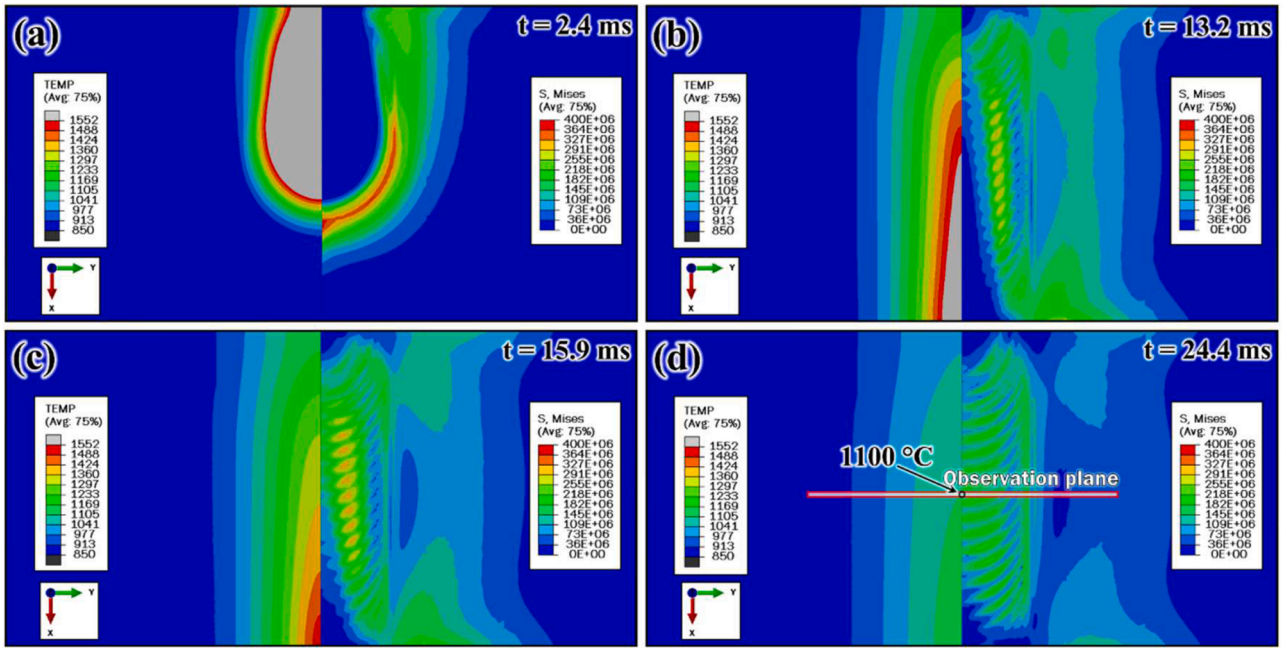

Fig. 14. Snapshot image of thermal-elastoplastic analysis of S-9 sample during solidification and cooling process; (a) $t = 2.4$ ms, (b) $t = 13.2$ ms, (c) $t = 15.9$ ms, (d) $t = 24.4$ ms. (Red box indicates the observation plane for residual stress analysis at the surface temperature of 1100 °C).

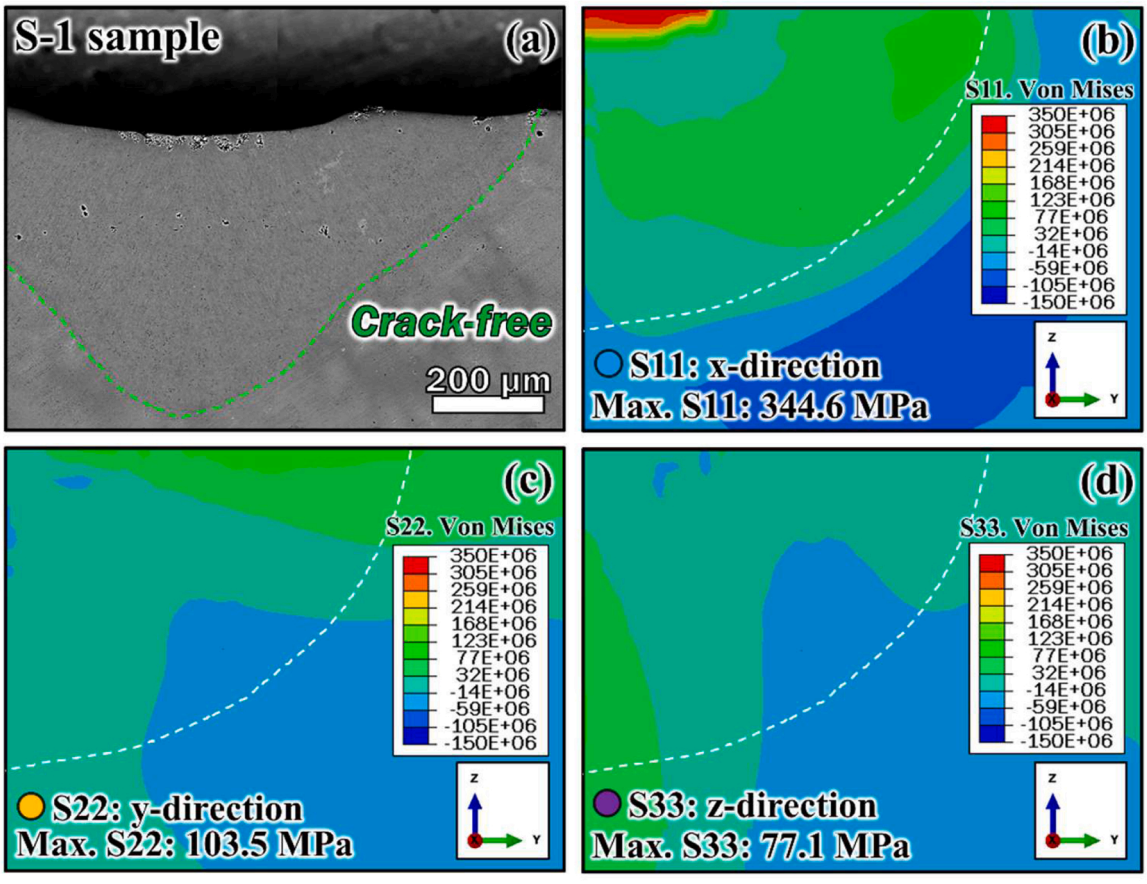

Fig. 15. (a) Cross-sectional image of single-track melted S-1 sample. Residual stress distribution of S-1 samples at 1100 °C color-coded by; (b) S11 (x-direction), (c) S22 (y-direction), (d) S33 (z-direction). (White dashed line represents the simulated melt pool boundary).

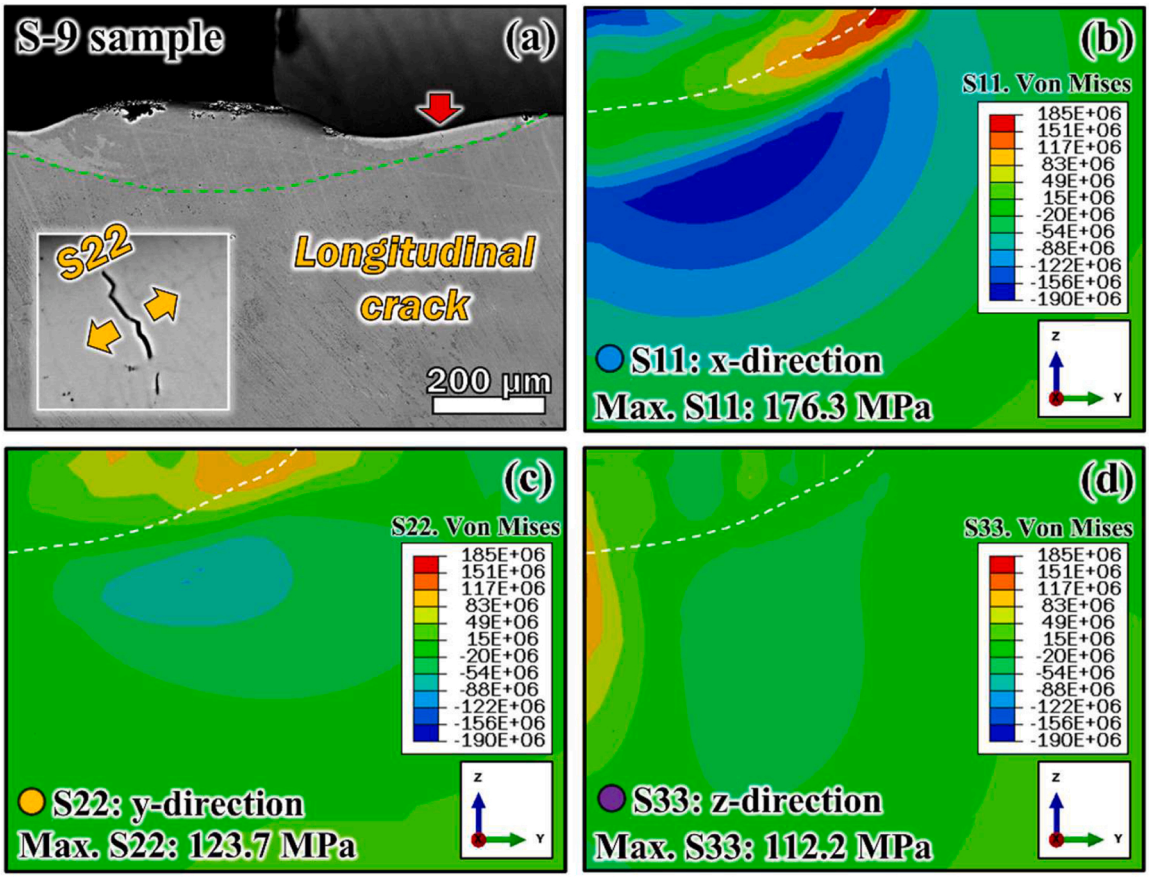

Fig. 16. (a) Cross-sectional image of single-track melted S-9 sample. Residual stress distribution of S-9 samples at 1100 °C color-coded by; (b) S11 (x-direction), (c) S22 (y-direction), (d) S33 (z-direction). (White dashed line and red arrow represent the simulated melt pool boundary and generated crack, respectively).

$$\mu = \frac{16}{15}\sqrt{\frac{m}{k_B T}\lambda} \tag{12}$$

where m is the atomic mass of the alloy, λ is the surface tension of the liquid, and k_B is the Boltzmann constant. Thus, the low preheating temperature leads to rapid cooling of the melt pool, and the liquid feeding could be limited due to the short lifetime of the liquid causing solidification cracking. In contrast, the dynamic viscosity could be more slowly increased due to the slow cooling rate by introducing preheating at 850 °C. Thus, a decreased cooling rate can increase the lifetime of the melt pool with low viscosity, and the solidification crack can be effectively suppressed by released solidification shrinkage tension and lack of liquid feeding (Nie et al., 2018). Furthermore, the temperature of the melt pool in the PBF-EB process is higher than that of the SLM process, which results in low surface tension and dynamic viscosity (Zhao et al., 2020). Therefore, the solidification crack in Ti-48Al-2Cr-2Nb alloys can be more suppressed in the PBF-EB process compared to the SLM process owing to the improved liquid feeding caused by the capillary effect.

As mentioned before, brittle cracking in single-track melted Ti-48Al-2Cr-2Nb alloys at 850 °C preheating was preferentially observed in the β/B2 phase region that was formed near the melt pool boundaries or surface edge region. The disordered β phase in TiAl alloy is more ductile than the α or γ phase owing to many slip systems, while the ordered B2 phase is extremely brittle owing to the intermetallic characteristic (Raji et al., 2020). The ductile behavior of the β phase in the Ti-45Al-7Nb-0.4 W-0.15B alloy was observed at 1200 °C, while brittle cracking occurred at 1000 °C in the compressive test (Liu et al., 2011). Liu et al. (2015a,b) reported that the B2 phase was much harder and more brittle than the α_2 and γ phases at low temperatures (ordering is B2 $>$ α_2 $>$ γ). This result indicates that the ordered B2 phase is the precursor of the crack opening of the Ti-48Al-2Cr-2Nb alloy at temperatures below $\beta \rightarrow$ B2 ordering, and cold cracking could be mainly attributed to the accumulated residual stress caused by rapid cooling after solidification. Therefore, it was clearly demonstrated that the dominant cracking mechanism of TiAl alloy was transitioned from solidification cracking to cold cracking by introducing the preheating at 850 °C. It has been reported that the β to B2 ordering in TiAl alloys varies depending on the composition in the temperature range of 1100–1200 °C (Kononikhina et al., 2017). To investigate the threshold of residual stress for crack opening of the B2 phase, the $\beta \rightarrow$ B2 ordering temperature of the Ti-48Al-2Cr-2Nb alloy was assumed to be 1100 °C.

3.6. Critical residual stress causing crack opening

A typical example of temperature and thermal stress fields during a single-track melting simulation is presented in Fig. 14a—d. The melted region with a temperature above the liquidus (1552 °C) had a gray threshold, and the residual stress of the melted region was reset to zero, as shown in Fig. 14a. The thermally induced stress accumulated in the solidification region because the temperature field was simultaneously changed by rapid cooling along the scan direction and caused complex compressive and tensile forces (Fig. 14b and c). When the temperature of the solidified region reached 1100 °C, the residual stress changed only slightly because of the slow cooling rate ($<1.68 \times 10^4$), as shown in Fig. 14d.

The von Mises stress according to the Cartesian coordination at 1100 °C were investigated to determine the critical residual stress causing crack opening in the B2 phase of the Ti-48Al-2Cr-2Nb alloy. The cross-sectional images and von Mises stress of single-track melted samples under various process parameters are presented in Figs. 15–18. The

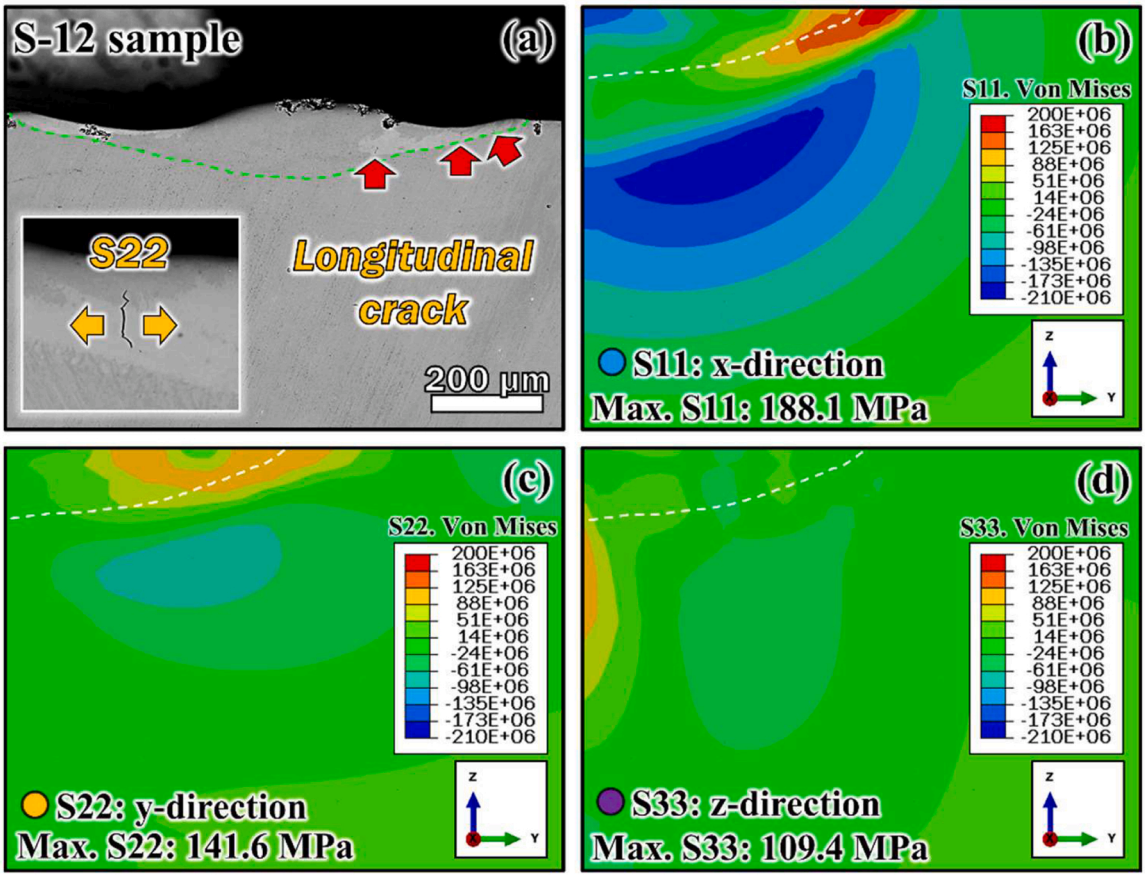

Fig. 17. (a) Cross-sectional image of single-track melted S-12 sample. Residual stress distribution of S-12 samples at 1100 °C color-coded by; (b) S11 (x-direction), (c) S22 (y-direction), (d) S33 (z-direction). (White dashed line and red arrow represent the simulated melt pool boundary and generated crack, respectively).

crack-free microstructure was obtained in the S-1 sample, while S11, which is a tensile stress along the scan direction (x-direction), was the highest at 344.6 MPa in the central melt pool region (Fig. 15a and b). This result demonstrates that brittle cracking by residual stress in the Ti-48Al-2Cr-2Nb alloy is restrained in the α dendritic region above the DBTT. The S11 values of all samples were higher than those of S22 and S33, indicating preferential crack opening perpendicular to the scan direction. Moreover, the S11 in the S-9, S-12, and S-17 samples were concentrated near the melt pool boundaries and surface edge region, which is well matched to the β/B2 dendritic region (Figs. 16b, 17b, 18b). Therefore, the transverse crack could primarily occur in the melt pool edge region due to the high residual stress along the scan direction, as shown in Fig. 5b—d. As the scan speed was raised to 600 mm/s, the S22 of the S-9 sample increased to 123.7 MPa with a longitudinal crack (Fig. 16a and b). The S22 in the S-12 and S-17 samples gradually increased with increasing scan speed at almost constant beam current, and the high S22 region was comparable to the crack opening region near the melt pool boundary and edge region (Fig. 17a, c and Fig. 18a, c). Interestingly, the crack initiation of S-12 and S-17 samples at the melt pool surface was suppressed compared to the melt pool boundary region despite comparable S11 and S22, as shown in Fig. 17a and Fig. 18a. In the thermal conduction model, the thermal energy dissipation was accelerated at the surface by the contribution of heat radiation, which cause the surface shrinkage and crack closure. Therefore, the crack initiation of S-12 and S-17 samples could be preferred at the melt pool boundary region owing to the high residual stress contributed by surface shrinkage.

The three building parameters, S-5, S-t, and S-6, were selected to investigate the crack opening threshold of the B2 phase at 1100 °C, as shown in Fig. 9c. The cross-sectional images and von Mises stress of the S-5 and S-6 samples after single-track melting are presented in Fig. 19a—h. Crack-free surfaces and cross-sectional microstructures were observed in S-5 sample (Fig. 19a and c). The maximum S11 and S22 in the melted region of the S-5 sample were determined to be 116.3 MPa and 109.8 MPa, respectively (Fig. 19b and d). On the other hand, transverse and longitudinal cracks were detected in the S-6 sample at the melt pool boundary region (Fig. 19e and g). In the solidification process, the high tensile stress along the scanning direction can result in strain hardening via dislocation accumulation, which suppresses the crack initiation along the y-direction. However, the longitudinal crack preferentially occurred at the β/B2 region of S-6 alloy despite the contribution of strain hardening. The S11 and S22 in the S-6 sample far increased to 188.2 MPa and 132.4 MPa as increasing cooling rate owing to decreased line energy (Fig. 19f and h). This result indicates that the cracking caused by residual stress of the Ti-48Al-2Cr-2Nb alloy is significantly affected by line energy, and it can be suppressed by process parameter optimization.

The maximum von Mises stress depending on the building parameters is shown in Fig. 20. The crack-free sample was obtained at residual stress below 110 MPa, while brittle cracking occurred at residual stresses above 123 MPa. To clarify the threshold residual stress of crack opening in the B2 phase, thermal-elastoplastic analysis was conducted at a scan speed of 357 mm/s and a beam current of 11 mA placed in the threshold boundary of the crack opening in the predicted crack density map (denoted as S-t), as shown in Fig. 9c. The highest S22 in the melt pool of the S-t sample was 117 MPa, which is within the range between the crack-free and crack opening samples. Therefore, the crack-free sample can be predicted by thermal-elastoplastic analysis using various building parameters, even though the microstructure had a brittle B2 phase in the Ti-48Al-2Cr-2Nb alloy. In conclusion, it was

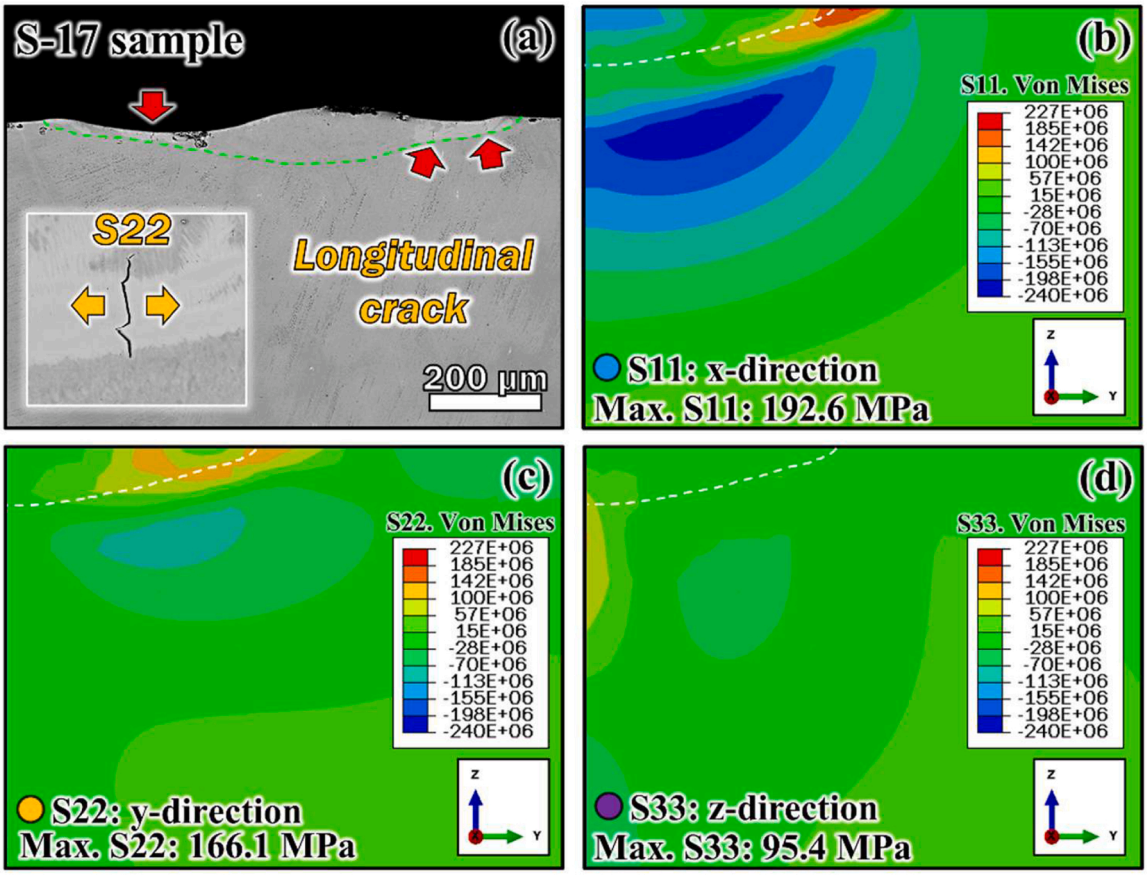

Fig. 18. (a) Cross-sectional image of single-track melted S-17 sample. Residual stress distribution of S-17 samples at 1100 °C color-coded by; (b) S11 (x-direction), (c) S22 (y-direction), (d) S33 (z-direction). (White dashed line and red arrow represent the simulated melt pool boundary and generated crack, respectively).

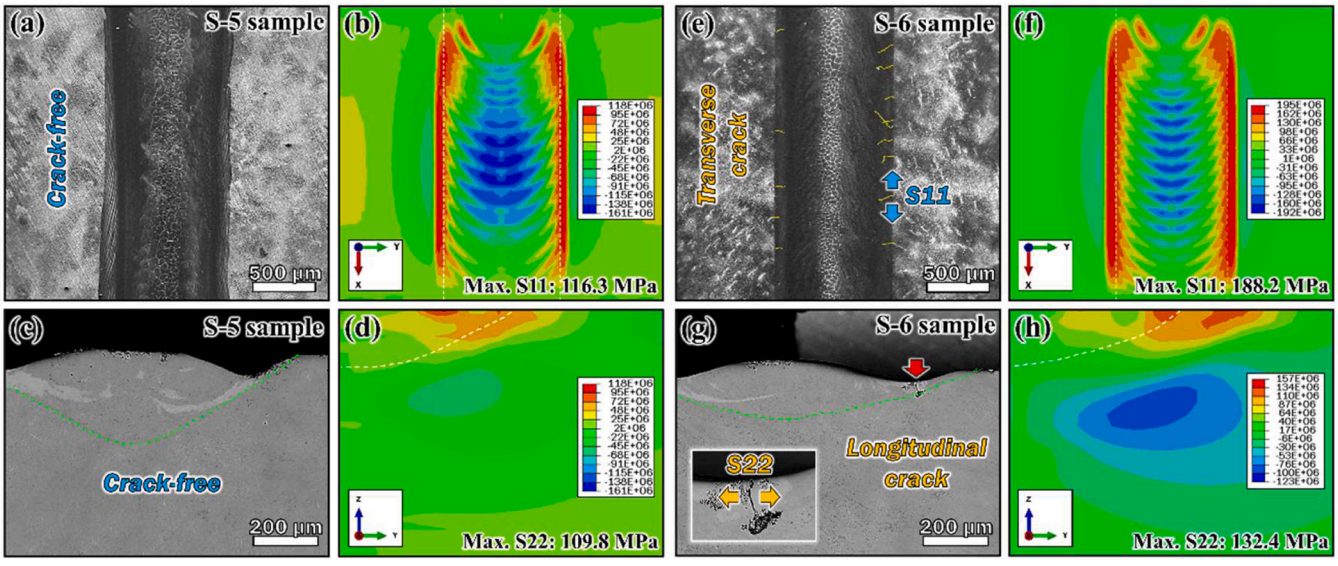

Fig. 19. Surface and cross-sectional BSE images of single-track melted Ti-48Al-2Cr-2Nb alloy; (a), (c) S-5 sample, (e), (g) S-6 sample. Residual stress distribution of single-track melted Ti-48Al-2Cr-2Nb alloy at 1100 °C; (b), (d) S-5 sample, (f), (h) S-6 sample.

demonstrated that the cracking caused by residual stress of the Ti-48Al-2Cr-2Nb alloy can be optimized by controlling the line energy above 1.85 J/mm.

4. Conclusion

The cracking mechanism of the Ti-48Al-2Cr-2Nb alloy in single-track melting at 850 °C preheating via powder bed fusion electron beam was investigated under various building parameters. The transverse crack after single-track melting was detected earlier than the longitudinal

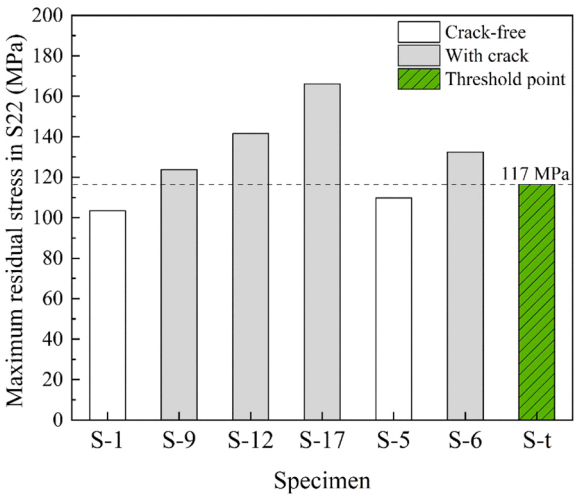

Fig. 20. Maximum von Mises stress in S22 of single-track melted Ti-48Al-2Cr-2Nb alloy at 1100 °C depending on building parameters.

crack, which could be due to the high tensile stress along the scan direction. The tensile strength of the single-track melted sample rapidly decreased as the crack density increased owing to interdendritic fracture. In the single-track melting of Ti-48Al-2Cr-2Nb at 850 °C preheating, the solidification crack was restricted due to improved liquid feeding by slow cooling, while crack opening was preferentially detected in the β/B2 region. A Scheil—Gulliver simulation revealed that the β dendrite regions with almost no α phase could be due to the restricted peritectic transformation of $L + \beta \rightarrow \alpha$ by rapid cooling above 2.3×10^4 K/s during solidification. The crack opening of Ti-48Al-2Cr-2Nb in the single-track melting at 850 °C preheating can be restricted by increasing the line energy above 1.85 J/mm. The critical residual stress causing the crack opening of the B2 phase at 1100 °C was determined to be 117 MPa via thermal-elastoplastic analysis. In conclusion, it is recommended that the β/B2 phase of the Ti-48Al-2Cr-2Nb alloy should be restricted by facilitating peritectic transformation in the solidification process to prevent residual stress-induced cold cracking in the powder bed fusion electron beam melting process at 850 °C preheating.

CRediT authorship contribution statement

Seungkyun Yim: Conceptualization, Methodology, Software, Validation, Formal analysis, Investigation, Writing - Original draft, Visualization, **Kenta Aoyagi:** Writing – review & editing, Supervision, Resources, **Huakang Bian:** Writing – review & editing, Supervision, Resources, **Keiji Yanagihara:** Investigation, Methodology, Validation, **Yuchao Lei:** Methodology, **Shin-ichi Kitamura:** Resources, **Hironobu Manabe:** Resources, **Yohei Daino:** Resources, **Kenta Yamanaka:** Writing – review & editing, Resources, **Akihiko Chiba:** Writing – review & editing, Supervision, Funding acquisition, Project administration.

Declaration of Competing Interest

The authors declare that they have no known competing financial interests or personal relationships that could have appeared to influence the work reported in this paper.

Data availability

The authors are unable or have chosen not to specify which data has been used.

Acknowledgments

This work was partially supported by JSPS KAKENHI through a Grant-in-Aid for Early-Career Scientists [grant number 21k14432]. This research was also partially supported by JSPS KAKENHI [grant number 18H05455]. This paper was based on results obtained from a project commissioned by the New Energy and Industrial Technology Development Organization (NEDO) [JPNP14014]. This work was partly supported by the Technology Research Association for Future Additive Manufacturing (TRAFAM). This work was also partly supported by the Innovative Structural Materials Association (ISMA) commissioned by the New Energy and Industrial Technology Development Organization (NEDO).

Appendix A. Supporting information

Supplementary data associated with this article can be found in the online version at doi:10.1016/j.jmatprotec.2023.118104.

References

Balla, V.K., Das, M., Mohammad, A., Al-Ahmari, A.M., 2016. Additive manufacturing of γ-TiAl: processing, microstructure, and properties. Adv. Eng. Mater. 18, 1208–1215. https://doi.org/10.1002/adem.201500588.

Caprio, L., Demir, A.G., Chiari, G., Previtali, B., 2020. Defect-free laser powder bed fusion of Ti–48Al–2Cr–2Nb with a high temperature inductive preheating system. J. Phys. Photonics 2, 0–12. https://doi.org/10.1088/2515-7647/ab7080.

Chiba, A., Daino, Y., Aoyagi, K., Yamanaka, K., 2021. Smoke suppression in electron beam melting of inconel 718 alloy powder based on insulator–metal transition of surface oxide film by mechanical stimulation. Materials. https://doi.org/10.3390/ma14164662.

Clemens, H., Kestler, H., 2000. Processing and applications of intermetallic γ-TiAl-based alloys. Adv. Eng. Mater. 2, 551–570. https://doi.org/10.1002/1527-2648(200009)2:9<551::AID-ADEM551>3.0.CO;2-U.

Clemens, H., Mayer, S., 2013. Design, processing, microstructure, properties, and applications of advanced intermetallic TiAl alloys. Adv. Eng. Mater. 15, 191–215. https://doi.org/10.1002/adem.201200231.

Deng, Q., Wu, Y., Wu, Q., Xue, Y., Zhang, Y., Peng, L., Ding, W., 2022. Microstructure evolution and mechanical properties of a high-strength Mg-10Gd-3Y–1Zn-0.4Zr alloy fabricated by laser powder bed fusion. Addit. Manuf. 49, 102517 https://doi.org/10.1016/j.addma.2021.102517.

Fang, K.T., Lin, D.K.J., Winker, P., Zhang, Y., 2000. Uniform design: theory and application. Technometrics 42, 237–248. https://doi.org/10.1080/00401706.2000.10486045.

Gao, P., Huang, W., Yang, H., Jing, G., Liu, Q., Wang, G., Wang, Z., Zeng, X., 2020a. Cracking behavior and control of β-solidifying Ti-40Al-9V-0.5Y alloy produced by selective laser melting. J. Mater. Sci. Technol. 39, 144–154. https://doi.org/10.1016/j.jmst.2019.08.026.

Gao, P., Huang, W., Yang, H., Jing, G., Liu, Q., Wang, G., Wang, Z., Zeng, X., 2020b. Cracking behavior and control of β-solidifying Ti-40Al-9V-0.5Y alloy produced by selective laser melting. J. Mater. Sci. Technol. 39, 144–154. https://doi.org/10.1016/j.jmst.2019.08.026.

Gäumann, M., Trivedi, R., Kurz, W., 1997. Nucleation ahead of the advancing interface in directional solidification. Mater. Sci. Eng. A 226–228, 763–769. https://doi.org/10.1016/s0921-5093(97)80081-0.

Graf, G., Rosigkeit, J., Krohmer, E., Staron, P., Krenn, R., Clemens, H., Spoerk-Erdely, P., 2021. In situ investigation of the rapid solidification behavior of intermetallic γ-TiAl-based alloys using high-energy X-ray diffraction. Adv. Eng. Mater. 2100557, 1–7. https://doi.org/10.1002/adem.202100557.

Gussone, J., Hagedorn, Y.C., Gherekhloo, H., Kasperovich, G., Merzouk, T., Hausmann, J., 2015. Microstructure of γ-titanium aluminide processed by selected laser melting at elevated temperatures. Intermetallics 66, 133–140. https://doi.org/10.1016/j.intermet.2015.07.005.

Gussone, J., Garces, G., Haubrich, J., Stark, A., Hagedorn, Y.C., Schell, N., Requena, G., 2017. Microstructure stability of γ-TiAl produced by selective laser melting. Scr. Mater. 130, 110–113. https://doi.org/10.1016/j.scriptamat.2016.11.028.

Juechter, V., Franke, M.M., Merenda, T., Stich, A., Körner, C., Singer, R.F., 2018. Additive manufacturing of Ti-45Al-4Nb-C by selective electron beam melting for automotive applications. Addit. Manuf. 22, 118–126. https://doi.org/10.1016/j.addma.2018.05.008.

Kim, Y.W., 1995. Effects of microstructure on the deformation and fracture of γ-TiAl alloys. Mater. Sci. Eng. A 192–193, 519–533. https://doi.org/10.1016/0921-5093(94)03271-8.

Kim, Y.W., Kim, S.L., 2018. Advances in gammalloy materials–processes–application technology: successes, dilemmas, and future. JOM 70, 553–560. https://doi.org/10.1007/s11837-018-2747-x.

Kononikhina, V., Stark, A., Gan, W., Schreyer, A., Pyczak, F., 2017. Ordering and disordering of β/βo-phase in γ-TiAl based alloys investigated by neutron diffraction. MRS Adv. 357, 1–6. https://doi.org/10.1557/adv.2017.145.

Körner, C., 2016. Additive manufacturing of metallic components by selective electron beam melting — a review. Int. Mater. Rev. 61, 361–377. https://doi.org/10.1080/09506608.2016.1176289.

Lee, S., Kim, J., Choe, J., Kim, S.W., Hong, J.K., Choi, Y.S., 2020. Understanding crack formation mechanisms of Ti–48Al–2Cr–2Nb single tracks during laser powder bed fusion. Met. Mater. Int. 78–91. https://doi.org/10.1007/s12540-020-00770-1.

Lei, Y., Aoyagi, K., Chiba, A., 2022. A method to manipulate non-steady-state columnar-to-equiaxed transition in powder bed fusion additive manufacturing using an electron beam. Acta Mater. 227, 117717 https://doi.org/10.1016/j.actamat.2022.117717.

Li, W., Liu, J., Zhou, Y., Li, S., Wen, S., Wei, Q., Yan, C., Shi, Y., 2016a. Effect of laser scanning speed on a Ti-45Al-2Cr-5Nb alloy processed by selective laser melting: Microstructure, phase and mechanical properties. J. Alloy. Compd. 688, 626–636. https://doi.org/10.1016/j.jallcom.2016.07.206.

Li, W., Liu, J., Zhou, Y., Wen, S., Wei, Q., Yan, C., Shi, Y., 2016b. Effect of substrate preheating on the texture, phase and nanohardness of a Ti-45Al-2Cr-5Nb alloy processed by selective laser melting. Scr. Mater. 118, 13–18. https://doi.org/10.1016/j.scriptamat.2016.02.022.

Liu, B., Liu, Y., Li, Y.P., Zhang, W., Chiba, A., 2011. Thermomechanical characterization of β-stabilized Ti-45Al-7Nb-0.4W-0. 15B alloy. Intermetallics 19, 1184–1190. https://doi.org/10.1016/j.intermet.2011.03.021.

Liu, G., Wang, Z., Fu, T., Li, Y., Liu, H., Li, T., Gong, M., Wang, G., 2015a. Study on the microstructure, phase transition and hardness for the TiAl-Nb alloy design during directional solidification. J. Alloy. Compd. 650, 45–52. https://doi.org/10.1016/j.jallcom.2015.07.259.

Liu, Y., Hu, R., Kou, H., Zhang, T., Wang, J., Li, J., 2015b. A mixture of massive and feathery microstructures of Ti48Al2Cr2Nb alloy by high undercooled solidification. Mater. Charact. 100, 104–107. https://doi.org/10.1016/j.matchar.2014.09.016.

Liu, Y., Hu, R., Zhang, T., Kou, H., Wang, J., Yang, G., Li, J., 2016. Dendritic growth and microstructure evolution with different cooling rates in Ti48Al2Cr2Nb alloy. J. Mater. Eng. Perform. 25, 38–45. https://doi.org/10.1007/s11665-015-1696-6.

Nie, X., Zhang, H., Zhu, H., Hu, Z., Ke, L., Zeng, X., 2018. Effect of Zr content on formability, microstructure and mechanical properties of selective laser melted Zr modified Al-4.24Cu-1.97Mg-0.56Mn alloys. J. Alloy. Compd. 764, 977–986. https://doi.org/10.1016/j.jallcom.2018.06.032.

Prasad Rambabu, N., Eswara Prasad, V.V.K., Wanhill, R.J.H., 2017. Aerospace materials and material technologies, Volume 1: aerospace material technologies. Aerosp. Mater. Mater. Technol. 1 (1), 586. https://doi.org/10.1007/978-981-10-2134-3.

Raji, S.A., Popoola, A.P.I., Pityana, S.L., Popoola, O.M., 2020. Characteristic effects of alloying elements on β solidifying titanium aluminides: a review. Heliyon 6. https://doi.org/10.1016/j.heliyon.2020.e04463.

Schimbäck, D., Braun, J., Leichtfried, G., Clemens, H., Mayer, S., 2021. Laser powder bed fusion of an engineering intermetallic TiAl alloy. Mater. Des. 201, 7–12. https://doi.org/10.1016/j.matdes.2021.109506.

Schwerdtfeger, J., Körner, C., 2014. Selective electron beam melting of Ti-48Al-2Nb-2Cr: microstructure and aluminium loss. Intermetallics 49, 29–35. https://doi.org/10.1016/j.intermet.2014.01.004.

Shi, X., Ma, S., Liu, C., Wu, Q., 2017. Parameter optimization for Ti-47Al-2Cr-2Nb in selective laser melting based on geometric characteristics of single scan tracks. Opt. Laser Technol. 90, 71–79. https://doi.org/10.1016/j.optlastec.2016.11.002.

Su, Y., Liu, C., Li, X., Guo, J., Li, B., Jia, J., Fu, H., 2005. Microstructure selection during the directionally peritectic solidification of Ti-Al binary system. Intermetallics 13, 267–274. https://doi.org/10.1016/j.intermet.2004.07.010.

Tetsui, T., 2011. Manufacturing technology for gamma-TiAl alloy in current and future applications. Rare Met. 30, 294–299. https://doi.org/10.1007/s12598-011-0288-3.

Vilaro, T., Thomas, M., Colin, C., Bertrand, P., Thivillon, L., Abed, S., Ji, V., Aubry, P., Peyre, P., Malot, T., 2010. Direct fabrication of a Ti-47Al-2Cr-2Nb alloy by selective laser melting and direct metal deposition processes 91, 586–591. https://doi.org/10.4028/www.scientific.net/AMR.89–91.586.

Wei, K., Wang, Z., Zeng, X., 2017. Preliminary investigation on selective laser melting of Ti-5Al-2.5Sn α-Ti alloy: From single tracks to bulk 3D components. J. Mater. Process. Technol. 244, 73–85. https://doi.org/10.1016/j.jmatprotec.2017.01.032.

Yan, L., Li, W., Chen, X., Zhang, Y., Newkirk, J., Liou, F., Dietrich, D., 2016. Simulation of cooling rate effects on Ti-48Al-2Cr-2Nb crack formation in direct laser deposition. In: Proceedings of the 27th Annual International Solid Freeform Fabrication (SFF) Symposium – An Additive Manufacturing Conference SFF 2016 680–690.

Yim, S., Bian, H., Aoyagi, K., Chiba, A., 2021. Effect of multi-stage heat treatment on mechanical properties and microstructure transformation of Ti–48Al–2Cr–2Nb alloy. Mater. Sci. Eng. A 816, 141321. https://doi.org/10.1016/j.msea.2021.141321.

Yim, S., Aoyagi, K., Yanagihara, K., Bian, H., Chiba, A., 2022a. Effect of mechanical ball milling on the electrical and powder bed properties of gas-atomized Ti–48Al–2Cr–2Nb and elucidation of the smoke mechanism in the powder bed fusion electron beam melting process. J. Mater. Sci. Technol. 137, 36–55. https://doi.org/10.1016/j.jmst.2022.07.024.

Yim, S., Bian, H., Aoyagi, K., Yanagihara, K., Kitamura, S. ichi, Manabe, H., Daino, Y., Hayasaka, Y., Yamanaka, K., Chiba, A., 2022b. Ball-milling treatment of gas-atomized Ti–48Al–2Cr–2Nb powder and its effect on preventing smoking during electron beam powder bed fusion building process. Addit. Manuf. 51, 102634 https://doi.org/10.1016/j.addma.2022.102634.

Zhao, Y., Koizumi, Y., Aoyagi, K., Wei, D., Yamanaka, K., Chiba, A., 2019. Molten pool behavior and effect of fluid flow on solidification conditions in selective electron beam melting (SEBM) of a biomedical Co-Cr-Mo alloy. Addit. Manuf. 26, 202–214. https://doi.org/10.1016/j.addma.2018.12.002.

Zhao, Y., Aoyagi, K., Yamanaka, K., Chiba, A., 2020. Role of operating and environmental conditions in determining molten pool dynamics during electron beam melting and selective laser melting. Addit. Manuf. 36, 101559 https://doi.org/10.1016/j.addma.2020.101559.

Zhu, D.D., Wang, H.W., Qi, J.Q., Zou, C.M., Wei, Z.J., 2012. Effect of Cr addition on microstructures and nanohardness of rapidly solidified Ti-48Al alloy. Mater. Sci. Technol. (U. Kingd.) 28, 1385–1390. https://doi.org/10.1179/1743284712Y.0000000087.